J. Fluid Mech. (2013), *vol.* 720, *pp.* 457–485.
doi:10.1017/jfm.2013.25

Flow over a flat plate with uniform inlet and incident coherent gusts

Imran Afgan[1,2,3,†], Sofiane Benhamadouche[4,5], Xingsi Han[1], Pierre Sagaut[1] and Dominique Laurence[2,4]

[1]Institut Jean Le Rond d'Alembert, Université Pierre et Marie Curie-Paris VI, 4 place Jussieu – case 162, 75252 Paris, France

[2]Modelling & Simulation Centre, School of MACE, University of Manchester, M13 9PL, UK

[3]Department of Mechanical & Aerospace Engineering, Air University, E-9, Islamabad

[4]Mécanique des Fluides Energies et Environnement (MFEE), EDF - R&D, 6 quai Watier, 78401 Chatou, France

[5]LaMSID, UMR CNRS EDF 2832, Clamart, France

(Received 17 February 2012; revised 7 November 2012; accepted 7 January 2013; first published online 27 February 2013)

The flow over a flat plate at a Reynolds number of 750 is numerically investigated via fine large-eddy simulation (LES), first at normal (90°) and then at oblique (45°) incidence flow direction with a uniform steady inlet. The results are in complete agreement with the direct numerical simulation (DNS) and experimental data, thereby serving as a validation for the present simulations. For the normal (90°) uniform inflow case, coherent vortices are alternately shed from both leading edges of the plate, whereas for the oblique (45°) uniform inflow case the vortices shed from the two sides of the plate interact strongly resulting in a quasi-periodic force response. The normal flat plate is then analysed with an incident gust signal with varying amplitude and time period. For these incident coherent gust cases, a reference test case with variable coherent inlet is first studied and the results are compared to a steady inlet simulation, with a detailed analysis of the flow behaviour and the wake response under the incident gust. Finally, the flat plate response to 16 different gust profiles is studied. A transient drag reconstruction for these incident coherent gust cases is then presented based on a frequency-dependent transfer function and phase spectrum analysis.

Key words: flow control, turbulent flows, vortex shedding

1. Introduction

Two-dimensional bluff bodies such as flat plates with large aspect ratios and infinite cylinders have served as geometrically simple, yet challenging, test cases for many fluid dynamics research studies. For such bluff bodies, the transient three-dimensional wake formation phenomenon can be analysed to understand other complex flow configurations. The flow past a flat plate at incidence has a fixed separation point where the Reynolds number (*Re*) only plays a role in the transition of the flow from laminar to fully turbulent; Norberg (2003), Thompson *et al.* (2006) and Afgan *et al.* (2007). Flow over such bluff bodies at high *Re* has been extensively investigated in the

† Email address for correspondence: afgan_imran@hotmail.com

past, mainly related to the aerospace industry (flow over nominally two-dimensional stalled wings). For lower *Re*, such flat-plate configurations have many other practical applications. For example, flow over solar panels or roadside signs/billboards, where knowing drag and other aerodynamics forces is of great importance. To provide some background, a few of the notable studies relating to such flows are cited here. Perhaps one of the earliest recorded studies is that conducted by Fage & Johansen (1927) in which the authors experimentally test a three-dimensional infinite flat plate with various angles of attack (0–90°) at a high *Re* of 1.5×10^5. The in-depth data reported in this study include the aerodynamic force response (C_L, C_D), velocity profiles along the edge of the plate and in the wake region, frequency of vortex shedding and vortex spacing. Perry & Steiner (1987) and Steiner & Perry (1987) present a two-part experimental study for flow over oblique and normal flat plates with different aspect ratios (5, 13.2 and 9.4) over an *Re* range of 14 000–20 000, discussing the qualitative quasi-averaged velocity fields in the wake. Kiya & Matsumura (1988) experimentally studied characteristics of various frequency components of the velocity fluctuations in the near wake behind a thin bevelled normal plate immersed in a uniform flow at *Re* of 23 000. The most important finding of their study was that the random shearing stress is mainly influenced by the components with frequencies of around half that of the vortex shedding frequency on the sides of the wake.

Another notable systematic three-part study is that of Najjar & Vanka (1995*a*,*b*) and Najjar & Balachandar (1998). In the first part the authors test a two-dimensional flat plate for *Re* ranging from 80 to 1000 using a finite-difference technique. In the second part (Najjar & Vanka 1995*b*), a similar three-dimensional configuration is studied by direct numerical simulation (DNS), with the underlying idea of correlating the aerodynamic coefficients and identifying the flow similarities between two- and three-dimensional flat-plate wake formations. Najjar & Balachandar (1998) further investigate via DNS the turbulent structure formation in the wake connected to the fluctuating drag and lift forces for a three-dimensional flat plate at *Re* of 250. They report a low-frequency unsteadiness at a period of about 10 times the vortex shedding period, resulting in a variation between low- and high-drag regimes. This is attributed to the imbalance of the streamwise and spanwise vortex formation which was found not to be in perfect synchronization.

For a flat plate with bevelled edges, Chen & Fang (1996) experimentally study the flow over an *Re* range of 3.5×10^3–3.2×10^4 for various angles of attack (0–90°). Yeung & Parkinson (1997) present an inviscid analytical model for steady separated flow around an inclined flat plate. Their model predictions are satisfactory only at small angles of attack where classical aerofoil theory is recovered. Mazharoğlu & Hacışevki (1999) experimentally test a normal flat plate at *Re* of 3.3×10^4 using triple decomposition of the instantaneous velocity into mean, coherent and turbulent parts. The decomposed velocity signals are then used directly for phase averaging thus easily highlighting the coherent structures in the wake region. Hussain (1986) discusses the characteristic measurement techniques of coherent structures in transitional and fully turbulent flows. Most of the aforementioned studies are very interesting from an academic point of point of view, presenting much insight into the flow field around bluff bodies. However, from an engineering perspective, for many practical applications, the incoming flow is neither uniform nor normal to the bluff body. Thus, one cannot directly correlate the flow behaviour to arbitrarily inclined bluff bodies with non-uniform inlet conditions, which have a far more complicated wake behaviour.

For unsteady flows, Koumoutsakos & Shiels (1996) simulated a normal impulsively started flat plate giving an in-depth description of the transient wake development and

the aerodynamic coefficients for a fairly low *Re*. However, no attempt was made in that study to look into the wake behaviour with an oscillatory inlet and/or model. Drabble *et al.* (1990) present a unique scenario relating the streamwise fluctuating forces on the flat plate with the inlet flow velocity fluctuations through a frequency-dependent transfer function called the admittance parameter. Though the admittance function is strongly dependent upon the geometric shape of the configuration, its response in the two incoming flow cases (turbulent and coherent), is reported to be quite the opposite. The present study tries to mimic this behaviour by introducing coherent yet varying gust signals: a series of coherent incident gusts superimposed on the mean inlet velocity. The response of the plate in terms of aerodynamic coefficients and aerodynamic admittance is then studied to understand the physics of the flow. A similar experimental study conducted on roadside signs by Quinn, Baker & Wright (2001) reports the aerodynamic forces and the wind admittance parameters. However, the authors do not discuss the underlying flow physics, let alone the profile of the inlet conditions or the plate response to it.

More recently Narasimhamurthy & Andersson (2009) performed a direct numerical simulation of flow over a normal flat plat at *Re* of 750 based on the plate width. The study concisely reports the Strouhal number, velocity profiles and Reynolds stresses in the wake region. For the uniform inlet cases of the current study (90° normal flat plate) comparisons are based on the data of this DNS of Narasimhamurthy & Andersson (2009). Other notable studies of similar configurations are those of Julien *et al.* (2003, 2004), Kim, Yang & Senda (2004), Wu *et al.* (2005), Saha (2007) and Nakagawa, Nitta & Senda (1999). A detailed table showing the tested configurations and summary of available results is presented in table 1.

The chosen test cases under uniform and unsteady inlet conditions are of interest from an engineering perspective: the stabilizing fins and rudders of sub-marines/ships (which experience varying angles of attack), down-force spoilers of race cars (naturally set at high oblique angles, 10°–35°), mixer grids in nuclear fuel rod bundles and wind turbines. Such geometrically similar configurations rarely experience an upstream uniform flow. In fact, the inflow conditions are strongly varying, for example the flapping wings of insects (which can be generalized as finite flat plates with sinusoidal or varying coherent inlets). Thus, from a practical point of view, it is of interest to not only study the flow over arbitrarily inclined configurations, but also to use the knowledge obtained to look at similar geometries with varying inflow conditions. Then, looking into a methodology for the response prediction of such complex cases would be a novel contribution to the field of fluid mechanics.

It is thus envisioned that the current paper will present a better understanding of flow over bluff bodies and their response to varying inlet conditions. The paper starts with the test case description and discussion of numerical treatment for simulations (§§ 2 and 3), followed by the discussion of results for uniform inlet cases (§ 4). Results for incident coherent cases are then presented in § 5. Finally, the fluctuating response and drag reconstruction are reported in § 6.

2. Case description

For the uniform inlet flow, two configurations have been numerically investigated: Case 1 is a normal flat plate with inflow angle of 90°; and Case 2 is an oblique plate at 45° to the inflow direction. The three-dimensionality of the wake formation for bluff bodies is attributed to the flow intrinsic and extrinsic effects as discussed in detail by Roshko (1993). A key parameter dictating the extrinsic effect is the aspect ratio (*AR*)

https://doi.org/10.1017/jfm.2013.25 Published online by Cambridge University Press

Study	Mode	*Re*	Geom	Angle (deg.)	Data reported
Fage & Johansen (1927)	Exp	1.5×10^5	Infinite 3D, *AR* 14	0–90	C_L, C_D, U/U_0 , Kármán vort. strength
Lamont & Hunt (1980)	Exp	—	Supersonic jet impingement	30–90	Surface pressure distributions, shock profiles
Perry & Steiner (1987)	Exp/Theo	20 000	2D, 3D, *AR* 5, 13.2, 9.4	45, 90	*St*, Blockage ratio, $\overline{U}$, $\overline{u_i'u_i'}$ contours
Steiner & Perry (1987)	Exp/Theo	20 000	2D, 3D, *AR* 5, 13.2, 9.4	45, 90	$\overline{U}$, $\overline{u_i'u_i'}$ profiles
Kiya & Matsumura (1988)	Exp	23 000	Bevelled 3D, *AR* 15	90	$\overline{U}$, $\overline{u_i'u_i'}$
Drabble *et al.* (1990)	Exp	20 000–100 000	3D, *AR* 1	90	Admittance parameter, C_L, C_D
Leder (1991)	Exp	2.8×10^4	3D	90	*St*, vortex shedding pattern
Dennis, Wang-Qiang & Launay (1993)	Exp/Num	100	Impulsively started 3D	—	Blockage effects, wake formation
Tamaddon-Jahromi, Townsend & Webster (1994)	Num	500	2D	90	Wake formation
Najjar & Vanka (1995*a*)	Num	1000	2D	90	C_L, C_D, U, *St*, Blockage effects
Najjar & Vanka (1995*b*)	Num	1000	3D	90	C_L, C_D, C_P
Chen & Fang (1996)	Exp	3.5×10^4	Bevelled 3D, *AR* 7.6	0–90	*St*, wake formation length
Koumoutsakos & Shiels (1996)	Num	20–1000	2D	90	C_D, vorticity contours, transient wake streamlines

TABLE 1. (Continued on next page)

https://doi.org/10.1017/jfm.2013.25 Published online by Cambridge University Press

Study	Mode	*Re*	Geom	Angle (deg.)	Data reported
Yeung & Parkinson (1997)	Analytical	—	—	0	St, C_P
Najjar & Balachandar (1998)	Exp/Num	250	2D, 3D	90	C_L, C_D , St
Mazharoğlu & Hacışevki (1999)	Exp	3.3×10^4	3D	90	1st-, 2nd- and 3rd-order statistics
Breuer & Jovicic (2001)	Num-LES	20 000	Infinite 3D	18	C_L, C_D , St
Julien, Lasheras & Chomaz (2003)	Exp	300	3D	—	Wake vortex formation plots
Julien, Ortiz & Chomaz (2004)	Analytical	—	—	—	Vortex street formation study
Wu *et al.* (2005)	Exp	18 000–27 000	Bevelled 3D, *AR* 4.7	90	St, $\overline{U}$, $\overline{u_i' u_i'}$
Saha (2007)	DNS	150	—	—	PDF, FFT, vorticity plots
Narasimhamurthy & Andersson (2009)	DNS	750	Infinite 3D	90	C_P, 1st-, 2nd- and 3rd-order statistics
Current study	Fine LES	750	Infinite 3D, variable inlets	90, 45	C_P, 1st-, 2nd- and 3rd-order statistics, admittance parameters, drag reconstruction

TABLE 1. Summary of notable experimental, numerical and analytical studies conducted to date for flow over a flat plate.

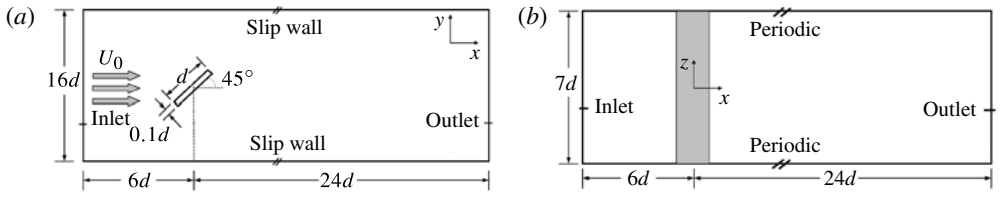

FIGURE 1. Flow configuration for oblique (45°) flat plate: (*a*) view in *XY* plane; (*b*) view in *XZ* plane.

of the bluff body as reported by Fox & West (1990) and Norberg (1994). Keeping this under consideration, a spanwise correlation of the streamwise (u) and cross-stream (v) velocities (not shown here) led to the conclusion that an AR of 7 was sufficient for the current configuration. The chord of the plate, d, and the thickness $0.1d$ were kept constant (see figure 1 for complete geometric details and boundary conditions).

Determination of an accurate gust model is a dynamic research topic; many stochastic and probabilistic approaches have been adopted in the past to present the gust behaviour, see Goyette, Brasseur & Beniston (2003), Bierbooms & Cheng (2002) and Bierbooms (2004). In the latter two, the authors present a stochastic approach to model gust for wind turbine designs. The gust-excited response of structures is discussed in detail and a probabilistic three-dimensional turbulence model for gust buffeting is presented by Solari & Piccardo (2000); the gust buffeting and turbulence uncertainties in atmospheric flows are then discussed by Pagnini & Solari (2002). In the current study, a realistic fit of the gust profile of Bierbooms & Cheng (2002) and Bierbooms (2004) is chosen as

$$u(t) = U_0 + A\frac{t^2\,(t-T)^2}{(T/2)^4}\sin\left(\frac{2\pi}{T}(3t+T)\right), \quad t \in [0, T], \tag{2.1}$$

where $A \in [0, 1]$ is the maximum gust amplitude (yielding a maximum U_{gust} of $2U_0$) and $T \in [0, 4.5]$ is the duration (time period) of the gust. This gust period is set to match the wind averaging periods. Generally, for a 10 min averaging period, a gust between 1 and 5 s is recommended, see Harper, Kepert & Ginger (2008) for more details. To discretize the gust model in two dimensions (A and T), an n-point Gauss–Legendre quadrature formula given by Press *et al.* (1996) is utilized.

Each incident gust cycle for the coherent inlet simulations is resolved over a fixed number of time steps: 1024. This leads to a strong dependence of the non-dimensional numerical time step ($\Delta t^+ = \Delta t U_0/d$) upon the time period of the gust oscillation (T). However, this ensures that each gust profile is adequately resolved, especially for the cases where the amplitude (A) is high and the time period (T) is very small. For the coherent inlet gust simulations, a reference gust test case is chosen, which is later used for comparison of mean statistics and instantaneous quantities with the uniform inlet case. Some characteristic gust profiles over the range of the chosen quadrature points in real space are shown in figure 2 with varying amplitude and time periods. A total of 16 large-eddy simulation (LES) runs were performed for different combinations of A and T where the time-dependent inlet boundary condition becomes a repetition of the same signal, thus leading to incident coherent gusts.

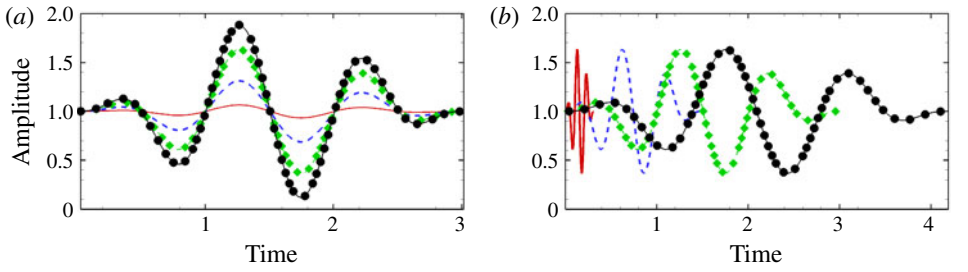

FIGURE 2. (Colour online) Gust profile for coherent inlet cases with varying gust amplitude (A) and time cycle (T): (*a*) different amplitudes (— $A1$, - - $A2$, -♦- $A3$, -●- $A4$) with constant time period ($T = 3.01$ s); (*b*) constant maximum amplitude ($A = 0.67$) with different time periods (— $T1$, - - $T2$, -♦- $T3$, -●- $T4$).

	Normal (90°) uniform inlet	Oblique (45°) uniform inlet	Normal (90°) coherent inlet
Coarse mesh (*CM*)	$7.6/96N_Z$, $Y^+ \approx 2$	$8.2/96N_Z$, $Y^+ \approx 2$	—
Medium mesh (*MM*)	$11.64/128N_Z$, $Y^+ < 1$	$12.14/128N_Z$, $Y^+ < 1$	$11.64/128N_Z$, $Y^+ < 1$
Fine mesh (*FM*)	$16.2/120N_Z Y^+ < 1$	$17.3/120N_Z$, $Y^+ < 1$	—
Very fine mesh (VFM)	$19.8/180N_Z$, $Y^+ < 1$	—	—

TABLE 2. Overview of the grid sensitivity study: case simulated, meshes tested in millions of cells/the total number of cells in the spanwise (N_Z) direction, maximum value of Y^+.

3. Numerical treatment

An incompressible collocated finite-volume code for complex geometries, *Code_Saturne* (Archambeau, Mchitoua & Sakiz 2004), is used to solve three-dimensional Navier–Stokes equations on unstructured grids. For LES, the standard Smagorinsky model with Van Driest wall damping function is used. A second-order pure central-differencing scheme is utilized for spatial discretization whereas the pressure–velocity coupling is ensured by the SIMPLEC algorithm (Van Doormal & Raithby 1984), with Rhie and Chow interpolation (see Rhie & Chow 1982) in the correction step to avoid oscillatory solutions. For temporal discretization, Crank–Nicolson scheme with linearized convection is used. For further details about the numerical treatment and *Code_Saturne* see Benhamadouche *et al.* (2005), Moulinec *et al.* (2005), Afgan *et al.* (2007).

To avoid needless refinement far from the plate, including the far wake, an O-grid was generated around the flat plate which was encapsulated inside a rectangular domain. The two-dimensional mesh was then extruded in the spanwise direction with uniform cell spacing. Such grid techniques have been suitably tested in the past, see Afgan *et al.* (2007). Three different meshes were tested: a coarse mesh (*CM*) with 7.6 million cells, a medium mesh (*MM*) with 11.6 million cells and a fine mesh (*FM*) with 16.2 million cells. The details of these meshes are given in table 2 along with maximum Y^+ values (non-dimensional distance to the wall) and the number of cells in

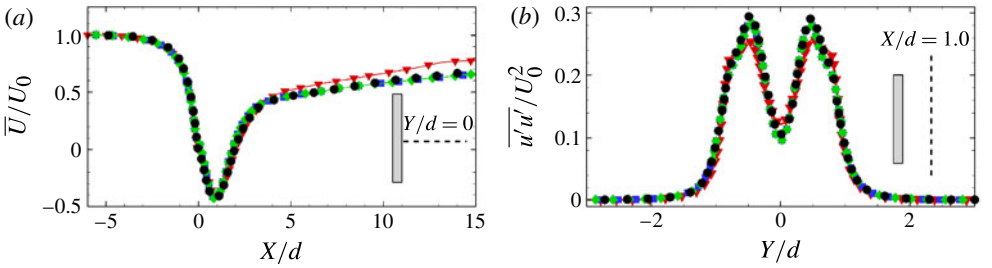

FIGURE 3. (Colour online) Comparisons of different meshes (−▼−,*CM*; −■−, *MM*; −♦−, *FM*) against ●, the DNS of Narasimhamurthy & Andersson (2009) for a normal flat plate with uniform inlet: (*a*) mean ($\overline{U}/U_0$) profile along symmetry line $Y/d = 0$ (*b*) streamwise Reynolds normal stress ($\overline{u'u'}/U_0$) profile along $X/d = 1.0$.

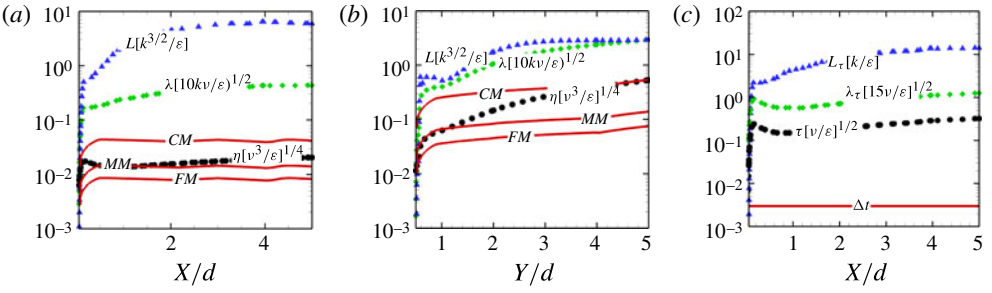

FIGURE 4. (Colour online) Comparisons between larger flow scales (−▲−, $L = k^{3/2}/\varepsilon$, $L_\tau = k/\varepsilon$), the Taylor scales (−♦−, $\lambda = (10\nu k/\varepsilon)^{1/2}$, $\lambda_\tau = (15\nu/\varepsilon)^{1/2}$), the Kolmogorov scales (●, $\eta = (\nu^3/\varepsilon)^{1/4}$, $\tau = (\nu/\varepsilon)^{1/2}$) and the grid scales ($\Delta$ and Δt) for the three meshes tested (*CM*, *MM* and *FM*). (*a*) Length scale comparison in the wake of the plate at $Y/d = 0.5$ along the X-axis. (*b*) Length scale comparison on the side of the plate at $X/d = 0$ along the Y-axis. (*c*) Time scale comparison.

the spanwise direction. The Y^+ distributions along the leeward surface and the side edge of the flat plate are always less than 1 for *MM*, *FM* and *VFM*. Figure 3 shows both mean velocity and Reynolds streamwise normal stress for all grids (*CM, MM* and *FM*) for the normal (90°) case with uniform inlet. It can be observed that no marked improvement in results is achieved by further refining the grid beyond *MM* resolution, especially in the plate wake region which is of interest in the current study. Hence, the medium mesh (*MM*) was taken as the benchmark resolution for all further simulations (both uniform and coherent inlet cases).

In addition to the grid sensitivity study, away from the body a spatial (grid) resolution estimation was also conducted by comparing larger flow length scales ($L = k^{3/2}/\varepsilon$), the Taylor length scales ($\lambda = (10\nu k/\varepsilon)^{1/2}$), the Kolmogorov scales ($\eta = (\nu^3/\varepsilon)^{1/4}$) and the space filter size ($\Delta = \mathrm{Vol}^{1/3}$) of the three meshes tested (*CM, MM* and *FM*). Here, k is the resolved turbulent kinetic energy computed as $k = (\overline{u'^2} + \overline{v'^2} + \overline{w'^2})/2$, ν is the viscosity and ε is the dissipation rate of kinetic energy defined as $\varepsilon = \varepsilon_{Vis} + \varepsilon_{SGS}$, where $\varepsilon_{Vis} \approx \nu\overline{(\partial u_i'/\partial x_j)(\partial u_i'/\partial x_j)}$ and $\varepsilon_{SGS} = \nu_t\overline{(\partial u_i'/\partial x_j)(\partial u_i'/\partial x_j)}$. Both k and ε have been computed for the medium mesh *MM* simulation. It is observed from figure 4(*a,b*) that *MM* is almost of the

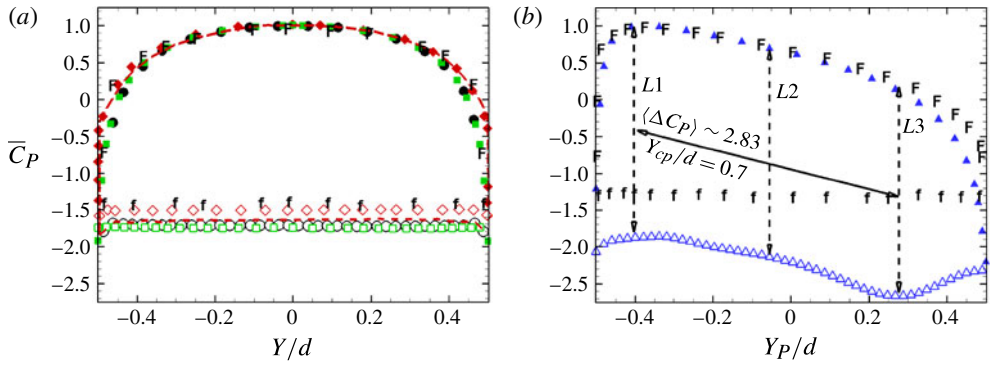

FIGURE 5. (Colour online) Mean C_P distribution on the surface of the plate: DNS (♦, front; ◇, back) Najjar & Vanka (1995*b*); DNS (●, front; ○, back) Narasimhamurthy & Andersson (2009); DNS (−, front; −−, back) Najjar & Balachandar (1998); experimental (-F-, front; -f-, back) Fage & Johansen (1927); LES normal plate with uniform inlet *MM* (■, front; □, back); LES oblique plate with uniform inlet *MM* (▲, front; △, back). (*a*) Normal (90°) flat plate. (*b*) Oblique (45°) flat plate.

same resolution as that of Kolmogorov scales both on the side of the plate and in its wake along the tip region. The present *MM* is considerably finer even in the spanwise direction when compared to the DNS studies of Moser & Balachandar (1998), Yao *et al.* (2001) and Narasimhamurthy & Andersson (2009). A similar estimation of the numerical time step is based on a comparison between integral time scales ($L_\tau = k/\varepsilon$), the Taylor time scales ($\lambda_\tau = (15\nu/\varepsilon)^{1/2}$) and the Kolmogorov time scales ($\tau = (\nu/\varepsilon)^{1/2}$), see figure 4(*c*). The effects of the subgrid-scale (SGS) contribution and dynamic model were also checked but the results are not presented here; see Afgan *et al.* (2011) for a detailed investigation of the SGS contribution with a similar numerical treatment.

The simulations were performed using a total of 2048 processors for each job on the Électricité de France (EDF) Blue Gene/P supercomputer for 150 CPU (central processing unit) hours, i.e. around 12 through-flow passes ($\mathrm{Pass}_F T = N\Delta t U_0/L_X$). For all uniform inlet cases, the flow was allowed to develop for 4 $\mathrm{Pass}_F T$ and averaged over the last 8 $\mathrm{Pass}_F T$. The total time-averaging period of the statistics translates into approximately 240 large-eddy turnover times ($t_e = D/U_0$). At the end of the simulations the results were also space averaged in the homogeneous (Z) direction. The simulations with incident coherent gusts were restarted from the uniform flow field and were run for at least 60 complete gust cycles which corresponds to about 6–9 $\mathrm{Pass}_F T$.

4. Results and discussion for uniform inlet cases

4.1. *Mean pressure distribution and aerodynamic forces*

The mean pressure coefficients ($\overline{C}_P = 2(\overline{P} - P_{ref})/\rho U_0^2$) for both normal (90°) and oblique (45°) cases (LES *MM*) with uniform inlet are shown in figure 5 compared to the measurements of Fage & Johansen (1927), DNS of Najjar & Vanka (1995*b*) at $Re = 1000$, Najjar & Balachandar (1998) at $Re = 250$ and Narasimhamurthy & Andersson (2009) at $Re = 750$. On the upstream surface (front-windward side) the current LES and DNS of Narasimhamurthy & Andersson (2009)

	Re	$St = fd/U_0$	$\overline{C}_D$	C'_D	$\overline{C}_L$	C'_L	L_R/d
Present LES 90°	750	0.167	2.29	0.251	6×10^{-5}	0.008	1.88
Narasimhamurthy & Andersson (2009) 90°	750	0.168	2.31	—	—	—	1.96
Najjar & Vanka (1995*b*) 90°	1000	0.143	2.26	—	—	—	2.55
Najjar & Balachandar (1998) 90°	250	0.161	2.36	—	—	—	2.35
Fage & Johansen (1927) 90°	1.5×10^5	0.146	2.13	—	—	—	—
Fage & Johansen (1927) 45°	1.5×10^5	0.205	1.80	—	—	—	—
Present LES 45°	750	0.206	1.95	0.328	1.83	0.562	0.62

TABLE 3. Comparisons between Strouhal number (St), mean drag and lift coefficients ($\overline{C}_D$, $\overline{C}_L$), r.m.s. of drag and lift coefficients (C'_D, C'_L) and mean recirculation length (L_R/d).

compare well, whereas the DNS of Najjar & Vanka (1995*b*) has a slightly wider mean pressure distribution especially near the edges of the flat plate. On the downstream surface (back-leeward side) once again the current LES and DNS of Narasimhamurthy & Andersson (2009) compare well, whereas the DNS of Najjar & Vanka (1995*b*) underpredicts the mean pressure distribution, which is complemented by an overprediction of the mean recirculation length, essentially leading to a lower Strouhal number (see table 3). Narasimhamurthy & Andersson (2009) attribute this discrepancy of higher pressure recovery in the DNS data of Najjar & Vanka (1995*b*) to a numerical artifact due to low grid resolution. For the oblique (45°) flat plate configuration the LES predictions on the pressure side compare well to the measurements of Fage & Johansen (1927) (49.85° flat plate), see figure 5(*b*). However, on the back surface the current LES shows a varying pressure change with a substantially lower plateau of around $\overline{C}_P = -2.2$. This difference in results is attributed to the very high Re used by Fage & Johansen (1927). It is interesting to note that the difference in mean pressure coefficient between the front and back surfaces (defined as $\Delta\overline{C}_P = (\overline{C}_P)_{front} - (\overline{C}_P)_{back}$) remains almost unchanged along the length of the flat plate, as shown by the vertical lines $L1$, $L2$ and $L3$ in figure 5(*b*).

The instantaneous lift ($C_L = 2F_L/\rho U_0^2 A$) and drag ($C_D = 2F_D/\rho U_0^2 A$) coefficients and their spectrum for both the cases are shown in figure 6, where A is the projected normal area. For the normal (90°) flat plate, a Strouhal number ($St = fd/U_0$) of 0.167 is found, which is in excellent agreement with the DNS of Narasimhamurthy & Andersson (2009) ($St = 0.168$), see table 3. The mean lift ($\overline{C}_L$) is close to zero showing that the first 3 digits of the other statistical results are meaningful. For the oblique (45°) flat plate, the mean lift ($\overline{C}_L$) and drag ($\overline{C}_D$) coefficients are −1.83 and 1.95, respectively. Observing figure 6(*b*), one notices a quasi-periodic force response for both the C_L and C_D profiles; this is attributed to the out-of-phase vortex pair

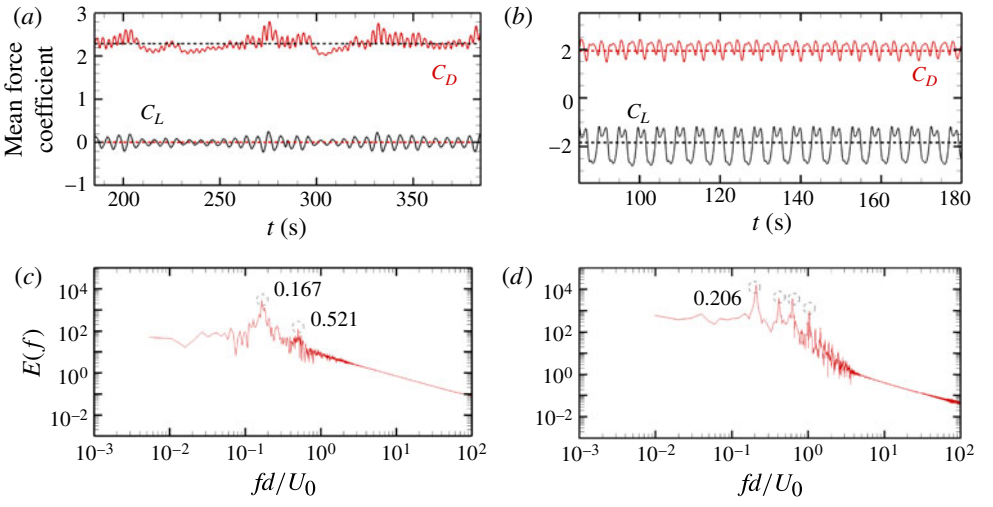

FIGURE 6. (Colour online) (*a*) Instantaneous lift (C_L, lower curve) and drag (C_D, upper curve) coefficients for normal 90° flat plate. (*b*) Instantaneous lift (C_L, lower curve) and drag (C_D, upper curve) coefficients for oblique 45° flat plate. (*c*) Power spectrum of C_L for normal 90° flat plate. (*d*) Power spectrum of C_L for oblique 45° flat plate.

shedding where the top and bottom vortices are shed at different frequencies leading to this multiple frequency/quasi-periodic force response. The lift force spectrum in figure 6(*d*), shows four pronounced shedding frequencies, the most energetic one corresponding to the principal vortex frequency with $St = 0.206$.

4.2. *Mean velocity profiles and wake vortex evolution*

The mean streamwise and cross-stream velocity profiles along the wake centreline for normal (90°) and oblique (45°) cases with a uniform inlet are shown in figures 7(*a*) and 7(*b*), respectively. In figure 7(*a*), for the normal (90°) case, the mean streamwise velocity ($\overline{U}_{90}/U_0$) has a maximum deficit of $0.44U_0$ and the mean recirculation length is $L_R/d = 1.88$. For the oblique (45°) case, this deficit is only $0.25U_0$, ∼50 % less than the normal (90°) case. The mean recirculation length is $L_R/d = 0.62$ as seen from the mean streamwise velocity ($\overline{U}/U_0$) in figure 7(*a*). On the other hand, the mean cross-stream velocity profile for the oblique (45°) case shows a complex flow behaviour along the wake centreline (see figure 7*b*). The sharp dip in mean cross-stream velocity and then a double peak higher plateau is an artifact due to plotting the velocity along the wake centreline (X-axis) as it is cutting through the main bigger vortex, Vor-D (see figure 7*d*).

For the normal (90°) configuration, the flow separates at both the lower and the upper leading edges of the plate, as expected from flow past any symmetric bluff body. However, for the oblique (45°) configuration, the flow exhibits a local separation at the top leading edge followed by a reattachment close to the trailing edge (see the streamlines of velocity around Vor-A in figure 7*d*); this is perhaps due to the 10 % thickness of the plate. After toppling over, the flow streamlines remain attached to the back surface of the plate until $Y/d = 0.25$, where the vortex is shed downstream. On the other hand, at the lower edge of the plate, the separation point is still located at the sharp leading edge, the origin point of Vor-C. This leads to the formation of several mean vortices in the plate wake, as indicated earlier and shown in the figure 7(*d*). The

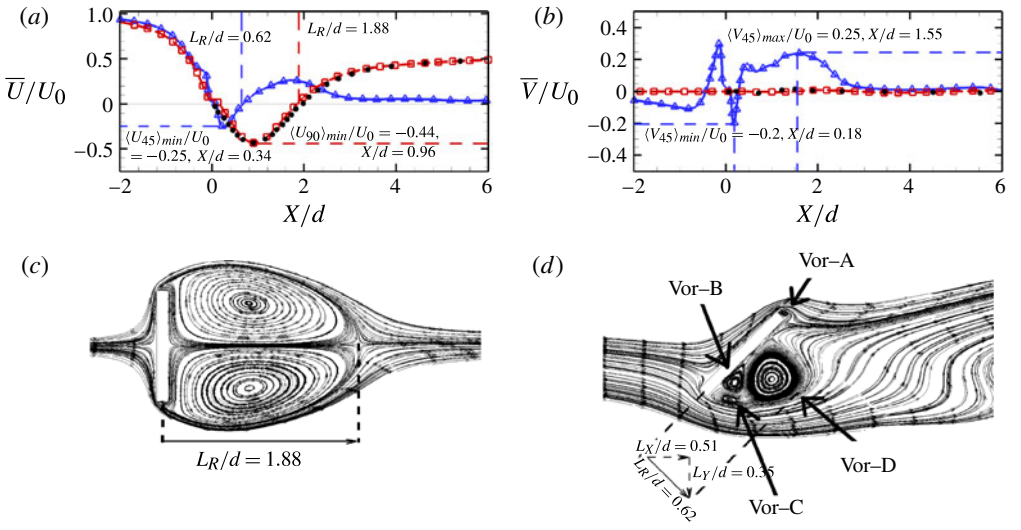

FIGURE 7. (*a*) Mean profile for streamwise velocity ($\overline{U}/U_0$); (*b*) mean profile for cross-stream velocity ($\overline{V}/U_0$): ●, Narasimhamurthy & Andersson (2009); □, LES normal (90°) case; △, LES oblique (45°) case. (*c*) Mean streamlines, LES normal (90°) case. (*d*) Mean streamlines, LES oblique (45°) case.

streamline patterns are similar to the experimental results of Perry & Steiner (1987) for the same configuration but at a much higher *Re*. The authors reported that clearly there was no antisymmetric vortex shedding, unlike the flow over a normal plate. In fact, the phase-integrated streamline pattern showed the existence of multiple saddle points and vortices in the wake, close to the current findings. However, they reported that the temporal mean velocity plots showed only a single mean vortex bubble at one end of the plate which was mainly attributed to the longer period that it stayed in the wake rather than the shedding from the other end.

The temporal evolution of these four wake vortices (Vor-A, Vor-B, Vor-C and Vor-D) can better be explained with the help of vorticity plots of figure 8. It is noted from figures 8(*a*) and 8(*h*) that the leading bottom edge of the plate gives rise to a main vortex (Vor-C, rotating counter-clockwise), which is then stretched along the leeward side of the plate into an ellipsoidal shape giving rise to a secondary vortex ($Vor - B$ rotating clockwise, see figures 8*c–e*). Meanwhile, at the top end of the plate there is a strong shear layer separation near the leading edge and then reattachment near the trailing edge, causing shedding of main vortex Vor-D (rotating clockwise, see figures 8*e,f*). This Vor-D structure also triggers generation of a secondary vortex (Vor-A rotating counter-clockwise, see figures 8*g,h*). However, Vor-A is more short lived as it is stretched and annihilated by the flow toppling over. What is interesting to note from the whole shedding cycle is that the two main vortices, Vor-C and Vor-D, shed from the opposite leading edges of the plate (figures 8*g–i* and *a–c*, respectively), each gives rise to a counter-rotating secondary vortex which is fairly short lived. However, both these secondary vortices are generated near the top trailing edge of the plate, which essentially means that the top of the plate generates three vortex sheddings, where as the bottom experiences only one vortex shedding. This is thought to be the main reason behind the quasi-periodic force response of the plate as a whole. The presence of a strong shear layer leads to the generation of these secondary

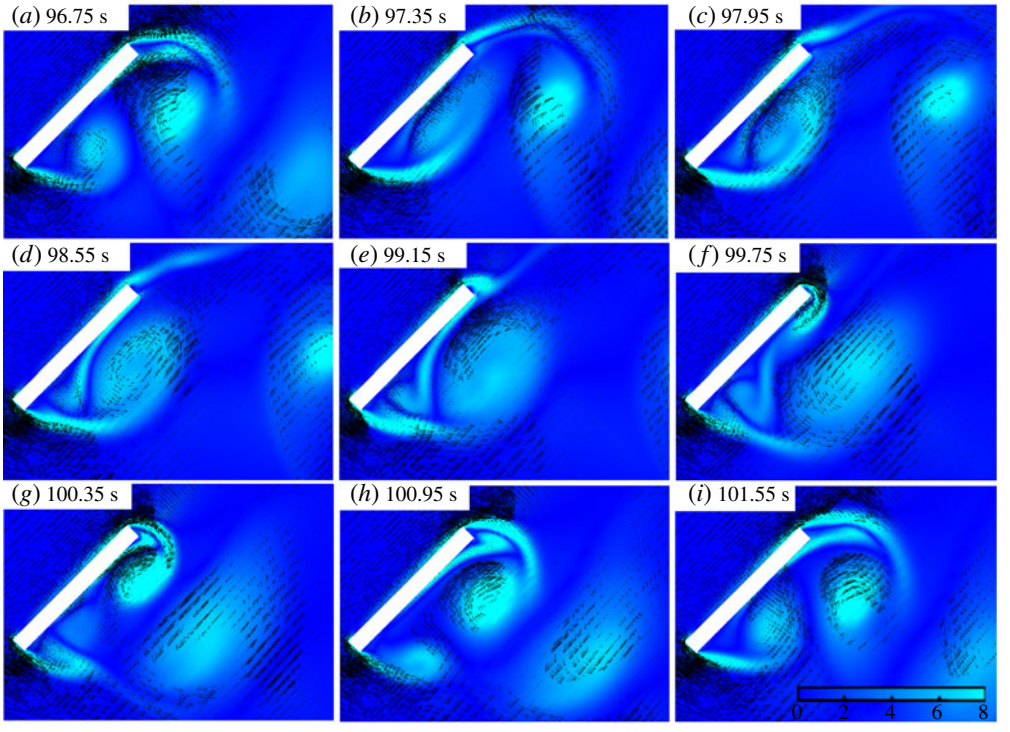

FIGURE 8. (Colour online) Near-wake vortex evolution: contours of vorticity superimposed with velocity vectors at different time instants as shown.

and additional smaller Kelvin–Helmholtz vortices, but these are short lived and of much higher frequency than the Kármán vortices. In fact, looking at the spectrum in figure 6(*d*), one observes higher frequency content, which is not seen in the normal (90°) case (figure 6*c*).

The mean streamwise ($\overline{U}/U_0$) and cross-stream ($\overline{V}/U_0$) velocity profiles at various downstream locations in the wake of the plate for both 90° and 45° incidences are shown in figure 9. For the 90° case, the maximum velocity deficit is close to $0.44U_0$ which is in good agreement with the DNS of Narasimhamurthy & Andersson (2009). Moving downstream, this deficit has now almost fully recovered at around $X/d = 2.0$, where the mean streamwise ($\overline{U}/U_0$) is close to zero. Thus, this location (also the end of the recirculation region) has been referred to as the free stagnation point in the past (see Fage & Johansen 1927 and Narasimhamurthy & Andersson 2009). It is further noted from figure 9(*a*) that the maximum streamwise ($\overline{U}/U_0 \approx 1.35$) velocity is located at around $Y/d \approx 1.0$ on the side of the plate along the line $X/d = 1.0$. After $X/d = 1.0$, a gradual decrease in the mean streamwise velocity outside the recirculation region and a deficit recovery inside the wake recirculation takes place. Turning to the mean cross-stream ($\overline{V}/U_0$) velocity profiles in figure 9(*b*) for the same normal (90°) case, one notices the existence of the largest cross-stream velocity magnitude of $\overline{V}/U_0 = 0.2$, which is again nearly located at the free stagnation point (along line $X/d = 2.0$). Moving downstream, one notices that the cross-stream velocity recovers back to zero at a much faster rate than the streamwise velocity (see figures 9(*a*) and 9(*b*)).

From the streamline pattern of figure 7(*c*) and the velocity profiles shown in figure 9(*b*), one notices that outside the recirculation region, the cross-stream ($\overline{V}/U_0$)

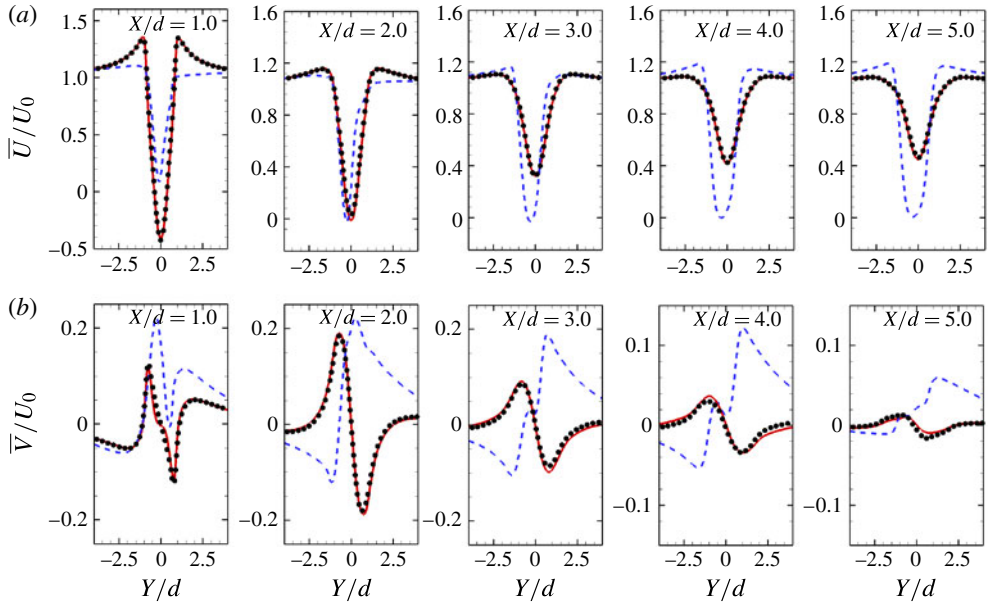

FIGURE 9. (Colour online) Mean velocity profiles along the height of the plate (●, Narasimhamurthy & Andersson (2009); —, LES normal (90°); −−, LES oblique (45°)) at various X/d downstream locations: (*a*) streamwise velocity ($\overline{U}/U_0$); (*b*) cross-stream velocity ($\overline{V}/U_0$).

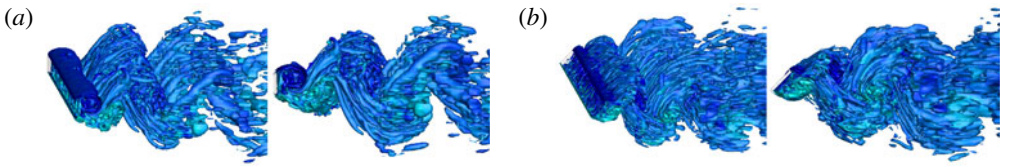

FIGURE 10. (Colour online) Isometric and side views of the IsoQ ($Q = -5(S_{ij}S_{ij} - \Omega_{ij}\Omega_{ij})$: (*a*) normal (90°) case, (*b*) oblique (45°) case.

velocity is directed away from the symmetry line (see the direction of $\overline{V}/U_0$ along the $X/d = 1.0$ line before $Y/d = -1.85$). However, inside and downstream of the recirculation region, the velocity is directed towards the symmetry line (notice the flow normality after the $X/d = 2.0$ line in figure 9*b*). For the oblique (45°) case, one observes a similar behaviour of $\overline{V}/U_0$ at or before the $X/d = 1.0$ line, where the flow is directed away from the symmetry line. However, moving downstream, this behaviour continues till $X/d = 7.5$ before the flow starts to be directed towards the symmetry plane (see the continued opposite response of $\overline{V}/U_0$ profiles along lines $X/d = 2, 3, 4$ and 5). This can also be judged from the streamlines of velocity behind the oblique (45°) plate shown in figure 7(*d*). For the uniform inlet cases, the mean Reynolds stress profiles, fluctuating kinetic energy (k/U_0^2) and decay of its dissipation rate ($\varepsilon\nu/U_0^4$) at various downstream locations were also compared to DNS of Narasimhamurthy & Andersson (2009) which are shown in appendix A.

In order to understand the wake formation behind the flat plate for both the normal (90°) and oblique (45°) configurations, instantaneous realizations of Q, the second invariant of the velocity gradient tensor, were calculated as shown in figure 10. For

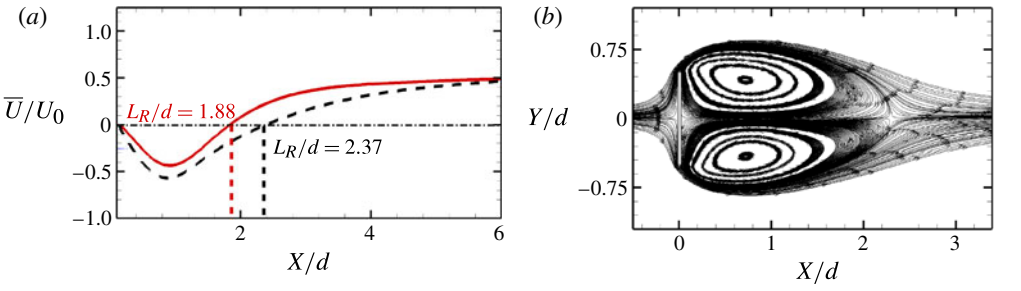

FIGURE 11. (Colour online) (*a*) Wake centreline mean streamwise velocity ($\overline{U}/U_0$): —, uniform inlet; and ––, coherent reference inlet wake velocities. (*b*) time-averaged velocity streamlines in the wake.

computations, Q is defined as $Q = -0.5(S_{ij}S_{ij} - \Omega_{ij}\Omega_{ij})$ (see Hunt, Wray & Moin 1988), herein normalized by $Q = \alpha\,(U_0/d)^2$, where S is the strain rate tensor, Ω is the rotation rate tensor and α is a non-dimensional constant set by the user in order to obtain desired flow structures (for the current cases α is chosen to return a value of $Q = 1/\mathrm{s}^2$). For the normal (90°) case, it is observed that the shear layer extrusion downstream before roll-up is around $1.5d$ and the shape of this top coherent structure is rather cylindrical, as can be seen from figure 10(*a*). On the other hand, the shear layer extrusion for the oblique (45°) case is around $1d$ as observed by the wake structure near the base of the plate in figure 10(*b*). The shape of this dominant structure before roll-up is elliptical rather than circular simply because of the flow angle of incidence.

5. Results and discussion for coherent inlet gust cases

From the range of simulations conducted, we now select and analyse a reference incident coherent gust case chosen at the central values of the limits $A_{ref}, T_{ref}[0.5, 2.25]$. The non-dimensional numerical time step ($\Delta t^+ = \Delta t U_0/d$) for this case is 0.00225, where $\Delta t = T_{ref}/1024$. All coherent inlet gust simulations were restarted from a fully developed uniform inlet case and were run for at least 60 complete incident gust periods (averaged over the last 40). A comparison of the resulting mean streamwise velocity profile ($\overline{U}/U_0$) in the wake centreline for this reference case (A_{ref}, T_{ref}) is shown in figure 11(*a*). It is observed that for this test case, the mean recirculation length (L_R/d) is 2.37, which is about 26 % longer than the uniform inlet case. The maximum velocity deficit has also increased to $0.56U_0$, approximately 27 % higher than in the uniform inlet case. The mean velocity streamline pattern for the (A_{ref}, T_{ref}) test case in the central (XY) plane presented in figure 11(*b*) shows that the flow behaviour in the mean sense, is similar to the uniform inlet case, where one observes the formation of two perfectly symmetrical vortices in the plate wake, again confirming sufficient time averaging.

Mean streamwise ($\overline{U}/U_0$) and cross-stream ($\overline{V}/U_0$) velocity profile comparisons between the A_{ref}, T_{ref} and the uniform inlet case at various downstream locations are shown in figure 12. For the uniform inlet case, the mean streamwise ($\overline{U}/U_0$) velocity along the wake centreline shows a complete recovery of the deficit at $X/D = 2.0$. However, for the A_{ref}, T_{ref} gust case, the free stagnation point is located further downstream ($X/D = 2.37$), as also seen by the streamline pattern of figure 11(*b*). Moving downstream in figure 12(*a*), one further observes that for the A_{ref}, T_{ref} gust

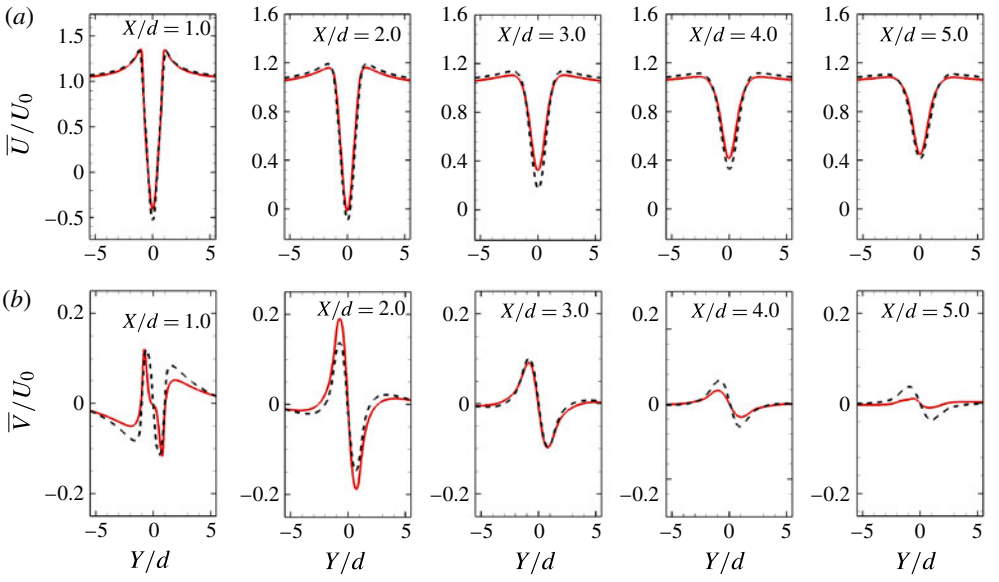

FIGURE 12. (Colour online) (*a*) Mean wake profiles for streamwise velocity ($\overline{U}/U_0$); (*b*) mean wake profiles for cross-stream velocity ($\overline{V}/U_0$): —, uniform inlet; and −−, coherent reference inlet.

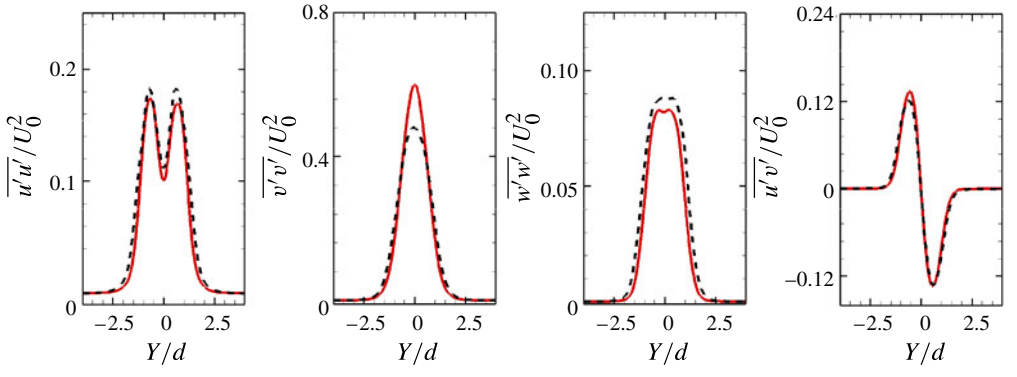

FIGURE 13. (Colour online) Comparisons between —, uniform inlet and −−, coherent reference inlet Reynold stresses at $X/d = 2.0$ downstream of the flat plate.

case, the velocity recovery is delayed as a whole. This is also visible from the lower slope of the velocity profile along the wake centreline in figure 11(*a*). On the other hand, the maximum mean cross-stream ($\overline{V}/U_0$) velocity for the A_{ref}, T_{ref} gust case is significantly lower than that of the uniform inlet case (see figure 12*b*). In fact, moving downstream, one observes that the cross-stream ($\overline{V}/U_0$) velocity for the two cases exactly overlap at $X/d = 3.0$. Furthermore, both upstream and downstream of this location, the A_{ref}, T_{ref} gust case shows a delayed increase and a delayed recovery, compared to the uniform inlet case. A comparison of Reynolds normal and shear stress profiles for the two cases along the free stagnation point location ($X/d = 2.0$) is shown in figure 13. Once again, it is observed that the streamwise ($\overline{u'u'}/U_0^2$) and spanwise ($\overline{w'w'}/U_0^2$) fluctuations are slightly higher for the A_{ref}, T_{ref} gust case, whereas

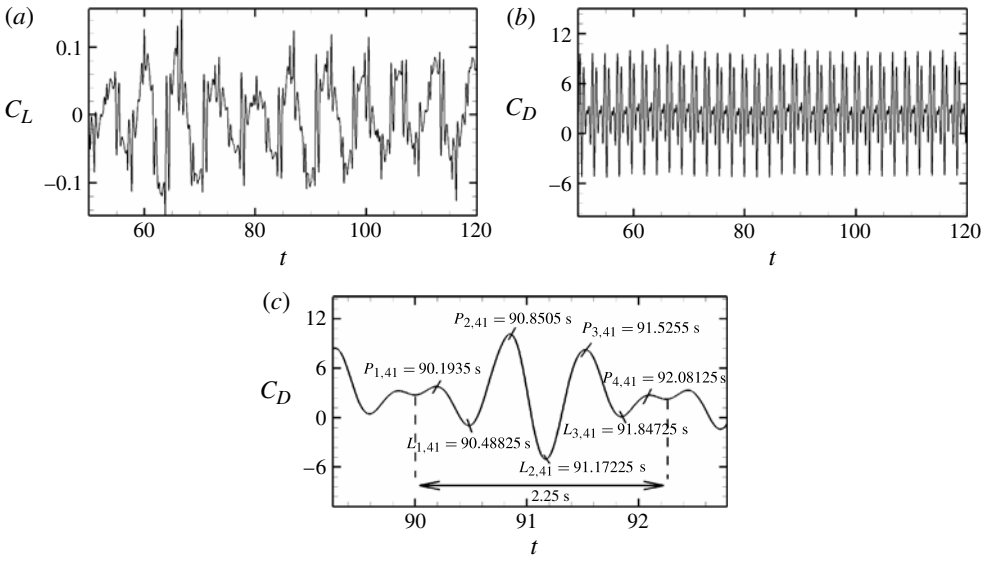

FIGURE 14. Aerodynamic force responses of the flat plate under coherent reference inlet conditions $[A, T] = [0.5, 2.25]$: (*a*) instantaneous lift (C_L); (*b*) instantaneous drag coefficient (C_D); (*c*) zoomed in instantaneous drag coefficient (C_D) for a single gust cycle ($N = 41$).

the cross-stream ($\overline{v'v'}/U_0^2$) fluctuations are substantially lower (observe the maximum cross-stream fluctuation level of approximately $0.48U_0$ for the A_{ref}, T_{ref} gust case in figure 13). The delay in cross-stream ($\overline{V}/U_0$) velocity and its substantially lower fluctuation levels ($\overline{v'v'}/U_0^2$) are due to the development of additional smaller vortices which are simultaneously shed from the sides of the plates in the A_{ref}, T_{ref} gust case; this flow behaviour is shown in figure 21 in Appendix B.

For the A_{ref}, T_{ref} gust case, instantaneous lift (C_L) and drag (C_D) responses for approximately 32 gust cycles are shown in figures 14(*a*) and 14(*b*), respectively. In figure 14(*c*), a zoomed-in instantaneous drag (C_D) response is shown for a single inlet gust cycle starting at time 90 s. The positive peaks in this figure are labelled as $P_{i,N}$ and the negative ones are labelled as $L_{i,N}$, where i is the peak number and N is the gust cycle number; in the current plot $N = 41$. At first glance, the instantaneous drag (C_D) response looks exactly like the inlet gust profile (see the profile shape of a single gust in figure 15*a*), with an additional maximum peak ($P_{4,N}$). However, the global drag cycle shown in figure 14(*c*) corresponds exactly to the time period of the inlet gust signal (2.25 s). In figure 14(*c*), one observes the two highest peaks of the drag (C_D) coefficient located at $P_{2,41} = 90.8505$ s and $P_{3,41} = 91.5255$ s. For any incident coherent gust case, one could in principle define the location of these peaks in a non-dimensional ($Pn_{i,N}$ or $Ln_{i,N}$) form as

$$Pn_{i,N} = \left(\frac{P_{i,N} - (N-1) \times T}{T} \right) \times 100, \tag{5.1a}$$

$$Ln_{i,N} = \left(\frac{L_{i,N} - (N-1) \times T}{T} \right) \times 100, \tag{5.1b}$$

where $Pn_{i,N}$ or $Ln_{i,N}$ is the non-dimensional location, $P_{i,N}$ or $L_{i,N}$ is the peak location, i is the peak number, N is the number of cycles or periods of gust and T is the time

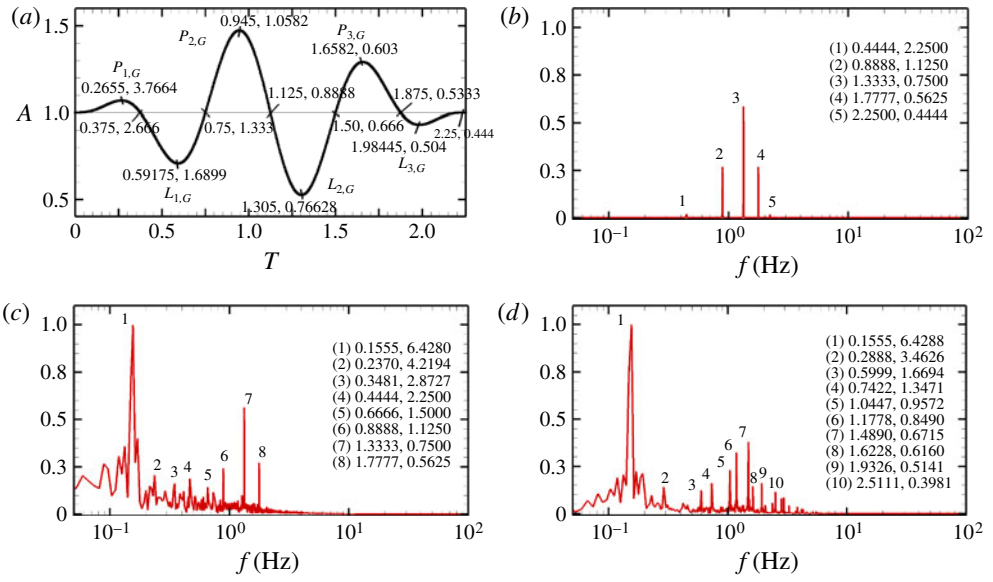

FIGURE 15. (Colour online) (*a*) Coherent reference inlet gust with $[A, T] = [0.5, 2.25]$. (*b*) PSD of the inlet pulse for 60 gust cycles. (*c*) PSD of the streamwise velocity component in the wake of the flat plate for a probe located at $X/d = 1.0$ and $Y/d = 0.5$. (*d*) PSD of lift signal of the flat plate. In (*b–d*) the most energetic peaks are numbered and displayed in three columns at top right, in the form of location number (#), frequency f (Hz) and time t (s) $= 1/f$ (Hz).

period of the gust. For the A_{ref}, T_{ref} gust case, the non-dimensional positive peaks two ($Pn_{2,41}$) and three ($Pn_{3,41}$) then become 37.8 and 67.8 %, respectively. Similarly, for the inlet gust signal (shown in figure 15*a*), one observes the global ($P_{2,G}$) and local ($P_{3,G}$) maxima locations at 0.945 s and 1.658 s, respectively, where the subscript G identifies that the associated signal is that of the inlet gust. By using (5.1*a*) and (5.1*b*), one obtains their non-dimensional counterparts as $Pn_{2,G} = 42\,\%$ and $Pn_{3,G} = 73\,\%$. Now the difference in the corresponding non-dimensional peaks between the inlet gust signal and the coherent reference case for any cycle can simply be calculated as

$$\Delta Pn_{i,N} = Pn_{i,G} - Pn_{i,N}, \tag{5.2a}$$

$$\Delta Ln_{i,N} = Ln_{i,G} - Ln_{i,N}. \tag{5.2b}$$

For example, for gust cycle 41, for the A_{ref}, T_{ref} gust case, the non-dimensional global ($\Delta Pn_{2,41}$) peak difference turns out to be 4.2 % and the non-dimensional local ($\Delta Ln_{3,41}$) peak difference turns out to be 5.2 %. Similar comparisons were made for a number of different cycles for the A_{ref}, T_{ref} gust case and it was found that the non-dimensional difference in any maximum or minimum peak never exceeds 6 % as can be seen from table 4. Similar observations were made regarding the maxima and minima peaks for all other coherent inlet cases and hence it was concluded that the lower frequencies (or larger structures) for any coherent inlet simulation exhibit a very similar response. This idea leads to the formulation of drag reconstruction, where one could in principle take the inlet gust formulation and the velocity record of a coherent inlet simulation and then predict the instantaneous drag response of another case with a similar coherent inlet. This is shown in detail later in § 6. There still remains one maximum peak ($P_{4,41}$), which can be seen in figure 14(*c*), which is additional to

N	$\Delta Pn_{1,N}$	$\Delta Pn_{2,N}$	$\Delta Pn_{3,N}$	$\Delta Ln_{1,N}$	$\Delta Ln_{2,N}$	$\Delta Ln_{3,N}$	$P_{4,N}$
31	4.2	4.5	5.0	2.3	4.7	5.3	92.9
41	3.2	4.2	5.2	1.6	5.9	6.0	92.5
60	4.0	5.5	4.6	3.4	5.2	5.7	92.4

TABLE 4. The non-dimensional difference in the maxima and minima peaks between the coherent reference A_{ref}, T_{ref} gust case and inlet gust signal at various gust cycles ($N = 31, 41, 60$).

the oscillations of the inlet flow. The existence of this additional peak in the drag response was seen to be consistent throughout all the tested coherent inlet cases. For the reference A_{ref}, T_{ref} incident coherent gust case, the non-dimensional location of this maximum peak is between 92 % and 93 % (see the last column of table 4.

The power spectrum density (PSD) of the inlet gust profile for the A_{ref}, T_{ref} test case is shown in figure 15(*b*). The PSD is taken from the Fourier transform of the velocity record of a probe far upstream of the flat plate for 60 complete gust cycles. As a validation, the spectrum of the inlet profile for 60 cycles was also plotted separately and no difference was found in the two curves. All the PSD in figures 15(*b–d*) are normalized by the magnitude of the most energetic frequency downstream of the flat plate (which is actually the non-dimensional Strouhal number of the plate). On each of figures 15(*b*), 15(*c*) and 15(*d*) the most energetic peaks are numbered and displayed at top right in the form of location number (#), frequency (f (Hz)) and time (t (s) $= 1/f$ (Hz)). Closely observing the inlet gust signal in figure 15(*a*) and its spectrum profile in figure 15(*b*), one notices that the inlet gust is actually a combination of a number of sine waves with changing amplitude. The frequencies identified as 1 and 5 are associated with the combined effect of the entire gust signal as $1/f_1$ leads to the time period of the gust ($t = 2.25$ s) and can be ignored or filtered out of the signal. The frequencies identified as 2 and 4 are due to half and quarter gust periods, whereas, the most energetic frequency observed in figure 15(*b*) is at location 3 (at $f = 1.3333$ Hz or $t = 1.125$ s), which is actually one-third the gust wave period.

In figure 15(*c*), the spectrum of the streamwise velocity signal of a probe downstream of the flat plate (at $X/d = 1.0$ and $Y/d = 0.5$) is shown. It is observed that the normal flat plate with the coherent reference incident gust exhibits a primary or most energetic frequency (also the Strouhal number) at location 1 ($f = 0.15555$), which is slightly lower than the Strouhal number of a flat plate with uniform inlet (0.1666). The three high peaks of the superimposed gust signal are still seen with little or no loss of the signal strength at locations 6, 7 and 8. The spectrum of the instantaneous lift signal of the flat plate for the same A_{ref}, T_{ref} gust case is shown in figure 15(*d*): peaks 1, 2 and 3 correspond to the primary, secondary and tertiary frequencies of the flat plate with uniform inlet (same as in figure 6*c*), whereas the additional peaks are either higher harmonics and/or constructive and destructive interference due to phase and amplitude differences between multiple wave fronts which combine to define a single gust signal. The time evolution of the complex vortex shedding in the wake of the plate for the same coherent A_{ref}, T_{ref} reference incident gust case is presented in figure 21 in Appendix B for three complete gust cycles. The shedding cycle time monitored by time evolution of the wake leads to almost the same shedding frequency of $f \approx 0.153$ which is very close to the global primary shedding frequency of 0.155. One could in principle perform a phase averaging based on the period of oscillations of the incident gust. However, as the

frequency of the inlet perturbations is much higher than the shedding frequency of the bluff body this will essentially wash out the underlying flow physics. Thus, the results for all current simulations are presented only averaged in time

6. Drag reconstruction

Till now, we have looked at the response and wake behaviour of a flat plate with uniform and unsteady incident coherent gusts. We now focus on quantifying the level of admittance or simply the disturbances which are added to the system with the inlet unsteadiness. This not only explains how the flow physics changes with upstream perturbations (strictly speaking not looking at small-scale inlet turbulent perturbations) but also enables one to quantify the level of unsteadiness thereby enabling the prediction of the bluff-body behaviour as a whole. Thus, this section deals with the fluctuating force measurements and drag reconstruction for the normal (90°) flat plate under the effect of incident coherent velocity fluctuations. The methodology for selection and implementation of the gust velocity profiles and the flow behaviour have already been discussed in § 2. Uniform steady flow over an object moving in-line with the flow is essentially equivalent to unsteady streamwise fluctuations over a stationary object, provided that the magnitude of the oscillations of the former (object) are equal to the streamwise fluctuations of the latter (flow) (Lighthill 1954). However, relative to the incoming flow, the body experiences an acceleration or a deceleration, leading to an added virtual mass which is basically the inertia added to or subtracted from the system due to the acceleration or deceleration. For such unsteady flows, there exists a strong and direct relationship between the flow fluctuations and the streamwise forces acting on the body. This relationship is generally represented in the form of a frequency-dependent transfer function, called the aerodynamic admittance function or simply admittance (see Drabble *et al.* 1990). The admittance function not only depends upon the nature of the flow instabilities but also on the geometric shape of the body. Furthermore, it is generally accepted that in a fully turbulent flow the admittance decreases if the frequency of the velocity fluctuations increase. On the other hand, for flows with coherent fluctuations, admittance increases directly as the frequency of the velocity fluctuations increase. For such coherent flows, admittance is defined by Vickery (1965) as

$$X^2(n) = 1 + \left(\frac{C_m}{C_D}\right)^2 \left(\frac{2\pi n d}{\overline{U}}\right)^2, \tag{6.1}$$

where C_D is the drag coefficient, C_m the virtual or added mass coefficient, n the frequency of the fluctuations, d the characteristic length scale and $\overline{U}$ the mean flow velocity. However, a more general representation in a non-dimensional form is given by Drabble *et al.* (1990):

$$X^2(n) = \frac{\overline{U}^2}{4\overline{F}^2} \left(\frac{S_F(n)}{S_u(n)}\right), \tag{6.2}$$

where $\overline{F}$ is the mean streamwise force acting on the body, $S_F(n)$ the power spectral density of the fluctuating force and $S_u(n)$ the power spectral density of the velocity fluctuations upstream of the flat plate. For fully coherent fluctuations, the admittance and aerodynamic response of the body is generally estimated by the *lattice* theory developed by Vickery (1965), later analysed in depth by Bearman (1971). The predictions of the lattice theory are valid only for configurations where the turbulent aspect ratio (defined as the ratio of the longitudinal integral scale of turbulence to the

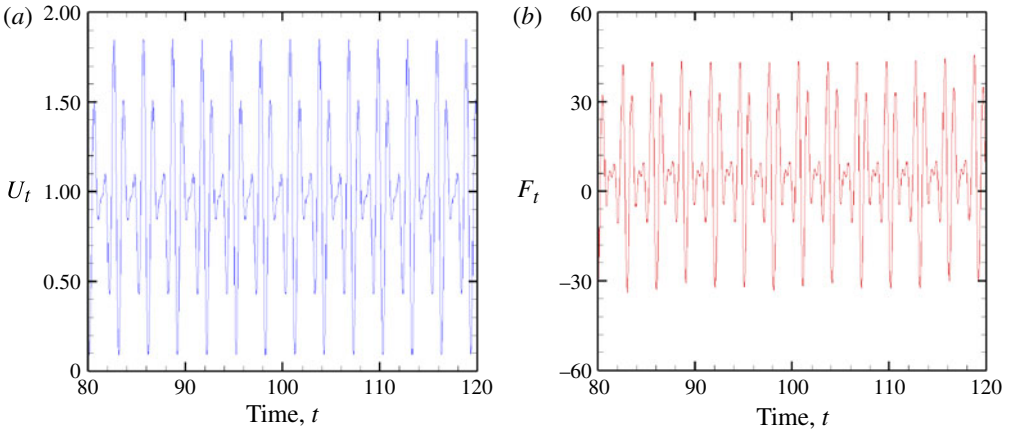

FIGURE 16. (Colour online) Incident coherent gust case A4T3: (*a*) instantaneous streamwise fluctuating velocity (U_t) profile at inlet (upstream of the plate); (*b*) computed fluctuating force response in the streamwise direction (F_t).

Case	$A_1(0.0694318)$	$A_2(0.3300094)$	$A_3(0.6699905)$	$A_4(0.9305681)$
$T_1(0.3124432)$	2.3133	2.3523	2.4907	2.5640
$T_2(1.4850426)$	2.3672	2.4382	2.5133	2.6091
$T_3(3.0149573)$	2.3681	2.5010	2.2530	2.6247
$T_4(4.1875567)$	2.3709	2.5410	2.5565	2.6538

TABLE 5. Mean drag ($\overline{C}_D$) calculated for the normal (90°) flat plate with coherent velocity inlets.

characteristic length scale) is sufficiently high (greater than 1.5). Further limitations lie in the fact that to apply the lattice theory both the shape and the length scale of turbulence need to be known *a priori*. To solve this dilemma, the general approach of assuming the turbulence to be isotropic leads to predictions which are quite crude (see Drabble *et al.* 1990). Thus, for the current study, the coherent inlet flow fluctuations are analysed with the aid of a methodology presented by Drabble *et al.* (1990). The aerodynamic admittance is computed along with the transient drag reconstruction on the basis of the frequency-dependent drag $C_D(\xi)$ and virtual mass $C_m(\xi)$ coefficients, where ξ is the non-dimensional frequency defined as $nd/\overline{U}$.

The 16 cases outlined in table 5 were restarted from a fully developed field using the results of the uniform inlet case. The resulting computed mean drag ($\overline{C}_D$) coefficients for each case are listed in table 5. It is interesting to note from table 5 that the mean drag is directly dependent, not only on the amplification of the coherent velocity, but also on the time period of the inlet gust cycle. Even though the mean drag ($\overline{C}_D$) shows a general increasing trend for higher amplitude of oscillations, the cases with smaller time periods show high r.m.s. values (not tabulated in this paper). In order to measure the velocity fluctuations, a number of probes were selected: upstream, on the side and in the wake of the plate. The instantaneous velocity signals for a probe upstream of the body for incident coherent gust case A4T3 is shown in figure 16(*a*). The resulting force response in the streamwise direction to the inlet velocity signal is reported in figure 16(*b*). From the trend of the velocity fluctuations

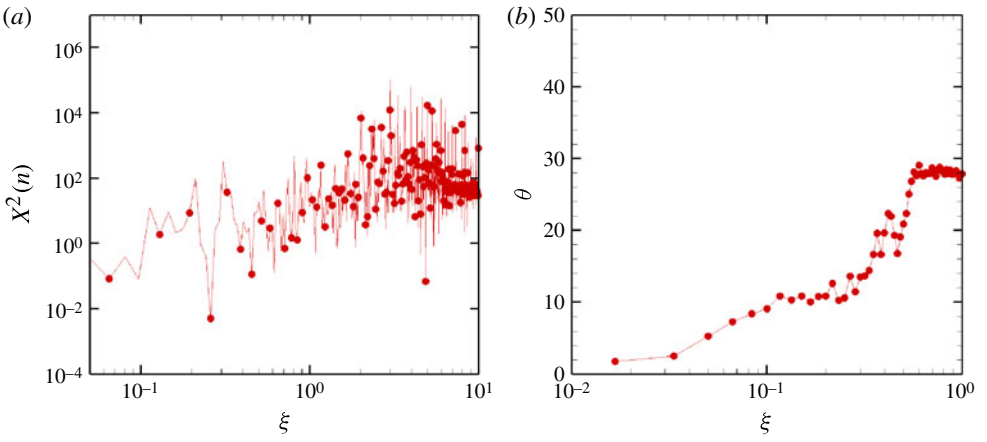

FIGURE 17. (Colour online) Incident coherent gust case A4T3: (*a*) admittance coefficient $(X^2(n) = (\overline{U}^2/4\overline{F}^2)(S_F(n)/S_u(n)))$; (*b*) phase angle between the fluctuating force and the fluctuating velocity against the non-dimensional frequency ($\xi = nd/\overline{U}$).

and the force response it can be safely assumed that the fluctuations are fully coherent as per the adopted inlet formulation. For all practical purposes for the calculation of the admittance coefficient $(X^2(n) = (\overline{U}^2/4\overline{F}^2)(S_F(n)/S_u(n)))$ experimentally, the spectrum of the velocity fluctuations $(S_u(n))$ is taken from a case in the absence of the plate model with no turbulent or coherent fluctuations in the flow. For the current study, the spectrum of velocity fluctuations from a probe upstream of the plate from the uniform inlet simulation is used instead. The spectrum for the fluctuating force $(S_F(n))$, on the other hand is calculated from the actual computed streamwise force response for the coherent inlet cases. The computed admittance coefficients for case A4T3 is shown in figure 17(*a*). It is observed that, for the coherent fluctuations, the admittance coefficient shows an increasing trend with an increase in the non-dimensional frequency, as reported by Drabble *et al.* (1990).

In the current cases, the coherence spectrum (as a function of non-dimensional frequency between the fluctuating velocity signal at a probe upstream of the flow and the fluctuating streamwise force) is utilized in identifying identical fundamental frequencies. The phase angle (θ) is then computed through the phase spectrum between the two (velocity and force response) signals for case A4T3 and is shown in figure 17(*b*). Since the phase angle is now a sort of measure between the inertial and drag forces, it shows an increasing trend with an increase in the non-dimensional frequency. It then follows from figure 17 that, for small phase (θ) angles, the drag component is dominant whereas for large (θ) the inertial component is dominant. This is logical since this means that when the flow structures are large, their effect on both the velocity signal and the drag response is similar leading to a closer coherence and a smaller phase difference between them. On the other hand, when the inertial components are large, the scales are smaller, showing a larger phase angle difference between the force response in the shape of the drag profile and the velocity signal. Similar behaviour is observed and reported by Drabble *et al.* (1990).

For fully coherent fluctuations as reported by Drabble *et al.* (1990), the total streamwise force acting in the plate can be represented as

$$F(t) = \frac{1}{2}\rho d^2 C_D u^2(t) + \rho d^3 C_m \frac{\mathrm{d}u(t)}{\mathrm{d}t}, \tag{6.3}$$

where the velocity signal ($u(t)$) can be decomposed into its mean ($\overline{U}$) and fluctuating (u') parts. The same concept when exploited for the total force leads to the decomposition of the total drag force ($F(t)$) into its mean ($\overline{F}$) and fluctuating ($\widetilde{F}$) components as

$$\overline{F} = \frac{1}{2}\rho d^2 C_D \left(\overline{U}^2 + \overline{(u')^2}\right), \tag{6.4a}$$

$$\widetilde{F} = \rho d^2 C_D \overline{U} u' + \rho d^3 C_m \frac{\mathrm{d}u'}{\mathrm{d}t}, \tag{6.4b}$$

where (6.4*b*) shows the contribution from both streamwise and inertial components of the force in the form of C_D and C_m respectively. Unfortunately, as pointed out by Davenport (1961, 1967), the drag component in (6.4*a*) needs to be the smooth drag (C_{Ds}) in the absence of any fluctuations, i.e. for uniform inlet flow. However, the drag (C_D) and virtual mass (C_m) components in (6.4*b*) are frequency dependent as they are associated with the fluctuating forces, i.e. ($C_D(\xi)$) and ($C_m(\xi)$) respectively. Thus, the true representation of the mean and fluctuating force components should be

$$\overline{F} = \frac{1}{2}\rho d^2 C_{Ds} \left(\overline{U}^2 + \overline{(u')^2}\right), \tag{6.5a}$$

$$\widetilde{F} = \rho d^2 C_D(\xi) \overline{U} u' + \rho d^3 C_m(\xi) \frac{\mathrm{d}u'}{\mathrm{d}t}. \tag{6.5b}$$

In the light of (6.5*a*) and (6.5*b*), the admittance as a function of frequency-dependent drag ($C_D(\xi)$) and virtual mass ($C_m(\xi)$) coefficients then becomes

$$X^2(n) = \frac{C_D^2(\xi)}{C_{Ds}^2}\left[1 + \left(\frac{2\pi n d}{\overline{U}}\right)^2 \frac{C_m^2(\xi)}{C_D^2(\xi)}\right], \tag{6.6a}$$

whereas the phase angle between the fluctuating velocity and the fluctuating force becomes

$$\theta(n) = \tan^{-1}\left[\frac{C_m(\xi)}{C_D(\xi)}\left(\frac{2\pi n d}{\overline{U}}\right)\right]. \tag{6.6b}$$

Now, since the admittance ($X^2(n)$) from (6.2), smooth drag coefficient (C_{Ds}) from a separate uniform inlet simulation and phase angle (θ) from coherence and phase spectrum are already known, one can compute the frequency-dependent drag ($C_D(\xi)$) and virtual mass ($C_m(\xi)$) coefficients from (6.6*a*) and (6.6*b*). These frequency-dependent $C_D(\xi)$ and $C_m(\xi)$ are shown against the non-dimensional frequency ($\xi = nd/\overline{U}$) for case A4T3 in figure 18(*a*). As expected, the drag ($C_D(\xi)$) and added mass or inertial ($C_m(\xi)$) components show an opposite trend with increasing non-dimensional frequency.

The stage is now set to predict or reconstruct the instantaneous drag response for the coherent inlet cases. This is done by choosing a fundamental (most energetic) frequency, in the current case a frequency close to the inlet oscillation time period, recording the values of ($C_D(\xi)$) and ($C_m(\xi)$) at this frequency, and using the appropriate velocity record of a separate coherent inlet simulation to solve (6.5*b*). The predicted fluctuating drag component for the case under discussion (A4T3) is shown in figure 18(*b*). The reconstructed mean drag for the A4T3 ($C_{Dp} = 2.458$) case was found to be in good agreement with the computed mean drag coefficient $C_D = 2.6247$. Interestingly, not only the mean drag ($\overline{C}_D$) values but also the instantaneous profiles are predicted quite accurately by only using a single fundamental frequency. One

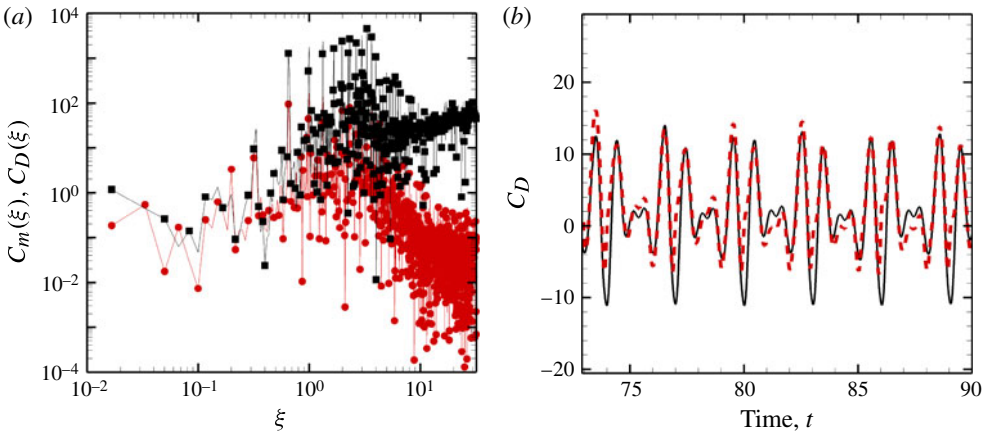

FIGURE 18. (Colour online) Incident coherent gust case A4T3: (*a*) frequency-dependent virtual mass (●, $C_m(\xi)$, lower profile) and drag (■, $C_D(\xi)$, upper profile) coefficients; (*b*) comparisons between the computed (—) and predicted (– –) drag (C_D) profiles using only the highest fundamental frequency of the actual velocity signal.

could in theory use multiple frequencies or even the entire velocity record of another simulation to improve the drag reconstruction. The most obvious advantage of drag reconstruction is that it can in principle be used as an uncertainty quantification tool to predict the fluctuating force response of a similar object subjected to coherent fluctuations or even the same configuration at a different time instant.

7. Conclusions

Flow over a normal (90°) and an oblique (45°) flat plate was numerically simulated with a uniform inlet. The normal (90°) case was also simulated with incident coherent velocity fluctuations. For the uniform inlet cases, the results were found to be in excellent agreement with the DNS and experimental data. For the normal (90°) uniform inlet case, alternate coherent vortex shedding was observed, whereas for the oblique (45°) uniform inlet case, the shedding from the two ends of the plate interacted strongly resulting in a quasi-periodic force response where the flow exhibited multiple frequencies in the wake. It is thus concluded that the complex wake behind oblique or inclined bluff bodies substantially differs from that of a normal bluff body where the thickness of the bluff body plays a key role.

The second half of the paper presents results for cases with fully coherent incident gusts where both the admittance and mean drag were computed. It is concluded that when the period of oscillation is short with high levels of amplitude of oscillations, the r.m.s fluctuations of the drag coefficient are higher. However, the mean drag and lift coefficients still show an increasing trend with an increase in the amplitude and time period of the oscillations. An attempt was made to reconstruct the drag following the method of Drabble *et al.* (1990) for some of the cases. The reconstructed transient drag and its mean were found to be in good agreement with the computed drag coefficient. It is thus concluded that one could in principle use the current methodology to predict, with reasonable accuracy, the response of a similar bluff body with unsteady incident coherent gusts. From an engineering perspective, this makes a novel contribution to the field of fluid mechanics, where one not only needs to access

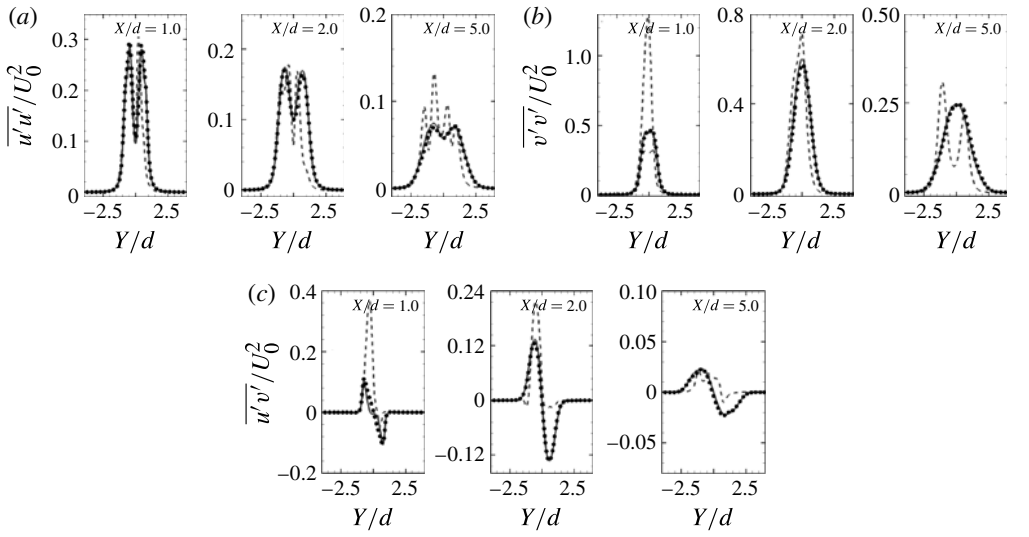

FIGURE 19. Mean Reynolds stress profiles (●, Narasimhamurthy & Andersson (2009); —, LES normal (90°); and −−, LES oblique (45°) configuration) at various downstream locations. (*a*) $\overline{u'u'}/U_0^2$, (*b*) $\overline{v'v'}/U_0^2$, (*c*) $\overline{u'v'}/U_0^2$.

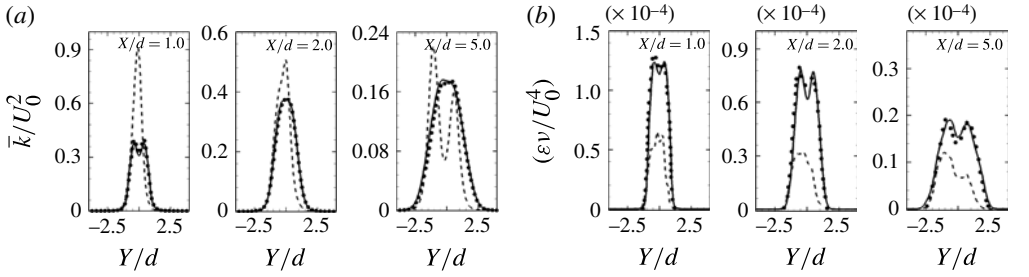

FIGURE 20. (*a*) Turbulent kinetic energy (k/U_0^2) and (*b*) dissipation rate of turbulent kinetic energy ($\varepsilon\nu/U_0^4$) at various downstream locations. ●, Narasimhamurthy & Andersson (2009); —, LES normal (90°); and −−, LES oblique (45°) configuration.

the wake behaviour under unsteady conditions, but also needs a formal tool or basis for its response prediction.

Acknowledgements

The authors would like to acknowledge the funding from French National Research Agency (*ANR*, *STURM-4*) and the continued funding by UK Research Council (*EPSRC*, *Computations for Advanced Reactor Engineering (CARE)*. We are also thankful to *Électricité de France* (EDF) for the computational resources and to Dr V. D. Narasimhamurthy for providing the DNS data for comparisons.

Appendix A. Reynolds stress, turbulent kinetic energy and dissipation for uniform inlet cases

Figures 19 and 20 show, for the uniform inlet cases, the mean Reynolds stress profiles, fluctuating kinetic energy (k/U_0^2) and decay of its dissipation rate ($\varepsilon\nu/U_0^4$)

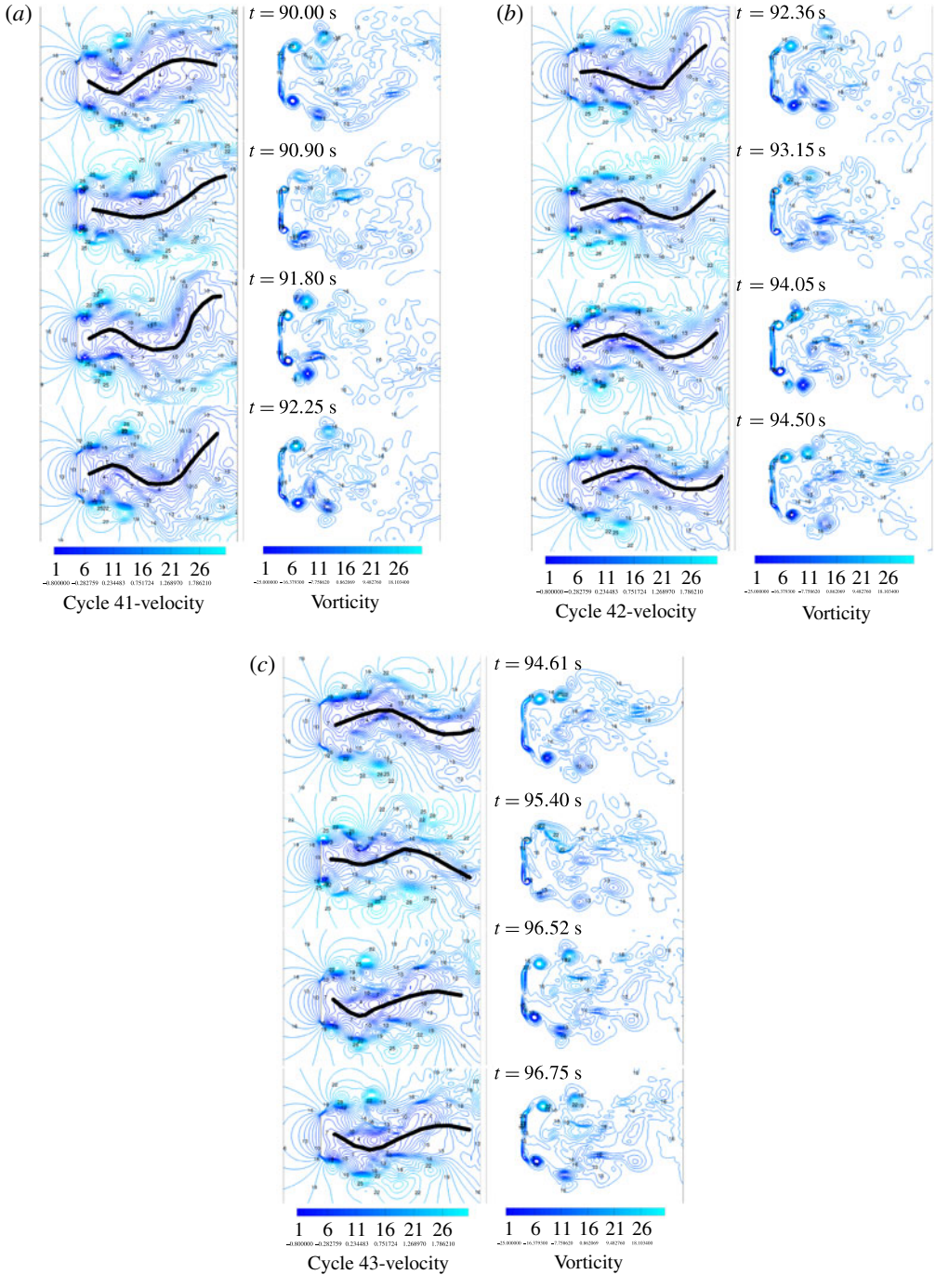

FIGURE 21. (Colour online) Comparison between instantaneous velocity (left) and vorticity contours (right) for the reference coherent inlet gust case ($A = 0.5$, $T = 2.25$) for three complete gust cycles, encapsulating one global shedding period: (*a*) gust cycle 41 staring at $t = 90.00$ s; (*b*) gust cycle 42 starting at $t = 92.36$ s; (*c*) gust cycle 43 starting at $t = 94.61$ s).

at various downstream locations, compared to the DNS of Narasimhamurthy & Andersson (2009).

Appendix B. Time evolution of vortices for incident coherent gust cases

The time evolution of the instantaneous velocity and complex vortex shedding in the wake of the plate for the coherent A_{ref}, T_{ref} reference incident gust case is presented in figure 21, encompassing 3 complete gusts.

REFERENCES

AFGAN, I., KAHIL, Y., BENHAMADOUCHE, S. & SAGAUT, P. 2011 Lareg Eddy Simulation of the flow around single and two side-by-side cylinders at subcritical Reynolds numbers. *Phys. Fluids* **23**, 075101.

AFGAN, I., MOULINEC, C., PROSSER, R. & LAURENCE, D. 2007 Large Eddy Simulation of turbulent flow for wall mounted cantilever cylinders of aspect ratio 6 and 10. *Intl J. Heat Fluid Flow* **28**, 561–574.

ARCHAMBEAU, F., MCHITOUA, N. & SAKIZ, M. 2004 Code_Saturne: a finite volume code for the computation of turbulent incompressible flows-industrial applications. *Intl J. Finite Vol.* **1**, ISSN 1634(0655).

BEARMAN, P. W. 1971 Investigation of forces on flat plate normal to a turbulent flow. *J. Fluid. Mech.* **46**, 177–198.

BENHAMADOUCHE, S., LAURENCE, D., JARRIN, N., AFGAN, I. & MOULINEC, C. 2005 Large Eddy Simulation of flow across in-line tube bundles. In *Nuclear Reactor Thermal Hydraulics, NURETH-11. Avignon, France. Paper* 405.

BIERBOOMS, W. 2004 A gust model for wind turbine design. *JSME Intl J.* B **47** (2), 378–386.

BIERBOOMS, W. & CHENG, P.-W. 2002 Stochastic gust model for design calculation of wind turbine. *J. Wind Engng Ind. Aerodyn.* **90**, 1237–1251.

BREUER, M. & JOVICIC, N. 2001 Separated flow around a flat plate at high incidence: an LES investigation. *J. Turbul.* **2** (18).

CHEN, J. M. & FANG, Y.-C. 1996 Strouhal numbers of inclined flat plates. *J. Wind Engng Ind. Aerodyn.* **61**, 99–112.

DAVENPORT, A. G. 1961 The application of statistical concepts to the wind loading of structures. *Proc. Inst. Civil Engrs* **19**, 449–472.

DAVENPORT, A. G. 1967 Gust loading factors. *J. Struct. Div.* **93** (3), 11–34.

DENNIS, S. C. R., WANG-QIANG, C. M. & LAUNAY, J. L. 1993 Viscous flow normal to a flat plate at moderate Reynolds numbers. *J. Fluid Mech.* **248**, 605–635.

DRABBLE, M. J., GRANT, I., ARMSTRONG, B. J. & BARNES, F. H. 1990 The aerodynamic admittance of a square plate in a flow with a fully coherent fluctuation. *Phys. Fluids* A **2** (6), 1005–1013.

FAGE, A. & JOHANSEN, F. C. 1927 On the flow of air behind an inclined flat plate of infinite span. *Proc. R. Soc. Lond.* A **116** (773), 170–197.

FOX, T. A. & WEST, G. S. 1990 On the use of end plates with circular cylinders. *Exp. Fluids* **9**, 231–239.

GOYETTE, S., BRASSEUR, O. & BENISTON, M. 2003 Application of a new wind gust parametrization: multi-scale case studies performed with the Canadian regional climate model. *J. Geophys. Res.* **108** (D13), 4374.

HARPER, B. A., KEPERT, J. D. & GINGER, J. D. 2008 Guidelines for converting between various wind averaging periods in tropical cyclone conditions. *World Meteorological Organization Report*. Appendix II.

HUNT, J. C. R., WRAY, A. A. & MOIN, P. 1988 Eddies, stream and convergence zones in turbulent flows. *Report* CTR-S88. Center for Turbulent Research, Stanford University.

HUSSAIN, A. K. M. F. 1986 Coherent structures and turbulence. *J. Fluid Mech.* **173**, 303–356.

JULIEN, S., LASHERAS, J. & CHOMAZ, J.-M. 2003 Three-dimensional instability and vorticity patters in the wake of a flat plate. *J. Fluid Mech.* **479**, 155–189.

JULIEN, S., ORTIZ, S. & CHOMAZ, J.-M. 2004 Secondary instability mechanisms in the wake of a flat plate. *Eur. J. Mech.* B/*Fluids* **23**, 157–165.

KIM, D. H., YANG, K. S. & SENDA, M. 2004 Large eddy simulation of turbulent flow past a square cylinder confined in a channel. *Comput. Fluids* **33**, 81–966.

KIYA, M. & MATSUMURA, M. 1988 Incoherent turbulence structure in the near wake of a normal plate. *J. Fluid Mech.* **190**, 157–165.

KOUMOUTSAKOS, P. & SHIELS, D. 1996 Simulations of the viscous flow normal to an impulsively started and uniformly accelerated flat plate. *J. Fluid Mech.* **328**, 177–227.

LAMONT, P. J. & HUNT, B. L. 1980 The impingement of underexpanded, axisymmetric jets on perpendicular and inclined flat plates. *J. Fluid Mech.* **100**, 471–511.

LEDER, A. 1991 Dynamics of fluid mixing in separated flows. *Phys. Fluids* A **3** (7), 1741–1748.

LIGHTHILL, M. J. 1954 The response of laminar skin friction and heat transfer to fluctuations in the stream velocity. *Proc. R. Soc. Lond.* A **224**, 1–23.

MAZHAROĞLU, Ç. & HACIŞEVKI, H. 1999 Coherent and incoherent flow structures behind a normal flat plate. *Exp. Therm. Fluid Sci.* **19**, 160–167.

MOSER, R. & BALACHANDAR, S. 1998 Self-similarity of time-evolving plane wakes. *J. Fluid Mech.* **367**, 255–289.

MOULINEC, C., BENHAMADOUCHE, S., LAURENCE, D. & PERIC, M. 2005 LES in a U-bend pipe meshed by polyhedral cells. In *ERCOFTAC ETMM-6 Conference*. Elsevier.

NAJJAR, F. M. & BALACHANDAR, S. 1998 Low frequency unsteadiness in the wake of a normal flat plate. *J. Fluid Mech.* **370**, 101–147.

NAJJAR, F. M. & VANKA, S. P. 1995*a* Simulations of the unsteady separated flow past a normal flat plate. *Intl J. Numer. Meth. Fluids* **21**, 525–547.

NAJJAR, F. M. & VANKA, S. P. 1995*b* Effects of intrinsic three-dimensionality on the drag characteristics of a normal flat plate. *Phys. Fluids* **7** (10), 2516–2518.

NAKAGAWA, S., NITTA, K. & SENDA, M. 1999 An experimental study on unsteady turbulent near wake of a rectangular cylinder in channel flow. *Exp. Fluids* **27** (3), 284–294.

NARASIMHAMURTHY, V. D. & ANDERSSON, H. I. 2009 Numerical simulation of the turbulent wake behind a normal flat plate. *Intl J. Heat Fluid Flow* **30**, 1037–1043.

NORBERG, C. 1994 An experimental investigation of the flow around a circular cylinder: influence of aspect ratio. *J. Fluid Mech.* **258**, 287–316.

NORBERG, C. 2003 Fluctuating lift on a circular cylinder: review and new measurements. *J. Fluids Struct.* **17**, 57–96.

PAGNINI, L. C. & SOLARI, G. 2002 Gust buffeting and turbulence uncertainties. *J. Wind Engng Ind. Aerodyn.* **90**, 441–459.

PERRY, A. E. & STEINER, T. R. 1987 Large-scale vortex structures in turbulent wakes behind bluff bodies. Part 1. Vortex formation processes. *J. Fluid Mech.* **174**, 233–270.

PRESS, W. H, TEUKOLSKY, S. A., VETTERLING, W. T. & FLANNERY, B. P. 1996 *Numerical Recipes in Fortran 77: Vol 1: The Art of Scientific Computing*, 2nd edn. Cambridge University Press, ISBN: 0-521-43064-X.

QUINN, A. D., BAKER, C. J. & WRIGHT, N. G. 2001 Wind and vehicle induced forces on flat plates–Part 1: wind induced force. *J. Wind Engng Ind. Aerodyn.* **89**, 817–829.

RHIE, C. & CHOW, W. 1982 A numerical study of the flow past an isolated aerofoil with trailing edge separation. *AIAA J.* **21**, 1525–1532.

ROSHKO, A. 1993 Prespectives on bluff body aerodynamics. *J. Wind Engng Ind. Aerodyn.* **49**, 79–100.

SAHA, A. K. 2007 Far-wake characteristics of two-dimensional flow past a normal flat plate. *Phys. Fluids* **19**, 128110.

SOLARI, G. & PICCARDO, G. 2000 Probabilistic 3-D turbulence modelling for gust buffeting of structures. *Prob. Engng Mech.* **16**, 73–86.

STEINER, T. R. & PERRY, A. E. 1987 Large-scale vortex structures in turbulent wakes behind buff bodies. Part 2. Far-wake structures. *J. Fluid Mech.* **174**, 271–298.

TAMADDON-JAHROMI, H. R., TOWNSEND, P. & WEBSTER, M. F. 1994 Unsteady viscous flow past a flat plate orthogonal to the flow. *Comput. Fluids* **23** (2), 433–446.

THOMPSON, M. C., HOURIGAN, K., RYAN, K. & SHEARD, G. J. 2006 Wake transition of two-dimensional cylinders and axisymmetric bluff bodies. *J. Fluids Struct.* **22**, 793–806.

VAN DOORMAL, J. P. & RAITHBY, G. D. 1984 Enhancements of the SIMPLE method for predicting incompressible fluid flows. *Numer. Heat Transfer* **7**, 147–163.

VICKERY, B. J. 1965 On the flow behind a coarse grid and its use as a model of atmospheric turbulence in studies related to wind loads in buildings. *National Physical Laboratory. Aero Rep. No.* 1143.

WU, S. J., MIAU, J. J., HU, C. C. & CHOU, J. H. 2005 On low-frequency modulations and three-dimensionality in vortex shedding behind a normal plate. *J. Fluid Mech.* **526**, 117–146.

YAO, Y. F., THOMAS, T. G., SANDHAM, N. D. & WILLIAMS, J. J. R. 2001 Direct numerical simulation of turbulent flow over a rectangular trailing edge. *Theor. Comput. Fluid Dyn.* **14**, 337–358.

YEUNG, W. W. H. & PARKINSON, G. V. 1997 On the steady separated flow around and inclined flat plate. *J. Fluid Mech.* **333**, 403–413.